Performance evaluation of the general characteristics based off-lattice Boltzmann scheme and DUGKS for low speed continuum flows

Lianhua Zhu, Peng Wang, Zhaoli Guo*

State Key Laboratory of Coal Combustion, Huazhong University of Science and Technology, Wuhan, 430074, China

Abstract

The general characteristics based off-lattice Boltzmann scheme proposed by Bardow et al., [1] (hereafter Bardow's scheme) and the discrete unified gas kinetic scheme (DUGKS) [2] are two methods that successfully overcome the time step restriction by the collision time, which is commonly seen in many other kinetic schemes. In this work, we first perform a theoretical analysis of the two schemes in the finite volume framework by comparing their numerical flux evaluations. It is found that the effect of collision term is considered in the evaluation of the cell interface distribution function in both schemes, which explains why they can overcome the time step restriction and can give accurate results even as the time step is much larger than the collision time. The difference between the two schemes lies in the treatment of the integral of the collision term when evaluating the cell interface distribution function, in which Bardow's scheme uses the rectangular rule while DUGKS uses the trapezoidal rule. The performance of the two schemes, i.e., accuracy, stability, and efficiency are then compared by simulating several two dimensional flows, including the unsteady Taylor-Green vortex flow, the steady lid-driven cavity flow, and the laminar boundary layer problem. It is observed that, DUGKS can give more accurate results than Bardow's scheme with a same mesh size. Furthermore, the numerical stability of Bardow's scheme decreases as the Courant-Friedrichs-Lewy (CFL) number approaches to 1, while the stability of DUGKS is not affected by the CFL number apparently as long as CFL < 1. It is also observed that DUGKS is twice as expensive as the Bardow's scheme with the same mesh size.

1. Introduction

The lattice Boltzmann method (LBM) has become a popular numerical tool for flow simulations. It solves the discrete velocity Boltzmann equation (DVBE) with sophistically chosen discrete velocity set. With the coupled discretization of velocity space and spatial space, the numerical treatment of convection term reduces to a very simple *streaming* process, which provides the benefits of low

---

*Corresponding author
Email address: zlguo@hust.edu.cn (Zhaoli Guo)

numerical dissipation, easy implementation, and high parallel computing efficiency. Another advantage of LBM is that, the simplified collision term is computed implicitly while implemented explicitly, which allows for a large time step even though the collision term causes stiffness at a small relaxation time. Although the time step in LBM is still restricted by the convection term due to the explicit nature of the streaming process, some preconditioning techniques [3, 4] and multigrid methods [5, 6] have be proposed to overcame this problem and have demonstrated their effectiveness for steady simulations. Those advantages makes the LBM a potential solver for high Reynolds number flows.

However, the coupled discretization of velocity and spatial spaces limits the LBM to the use of uniform Cartesian meshes, which prohibits its applications for practical engineering problems evolving complex geometry. The coupling also restricts the choice of discrete velocities, namely the discrete velocities have to be integer values and fitted to spatial lattices. But for compressible flows, micro or rarefied flows and multicomponent flows, it is desirable to use more general and even irrational discrete velocities that can not be fitted to spatial lattices. Actually, there have been some efforts to extend the standard discrete velocity families to higher order velocity models [7, 8, 9, 10].

Some efforts have been made to extend the standard LBM to non-regular (non-uniform, unstructured) meshes, and a number of so called off-lattice Boltzmann (OLB) methods have been developed by solving the DVBE using certain finite-difference, finite-volume, or finite-element schemes [11, 12, 1, 13, 14, 15, 16, 17, 18, 19, 20]. These OLB schemes differ from each other in the temporal and spatial discretizations. However, a straightforward implementation of the CFD techniques usually leads to the loss of the advantages of standard LBM, especially the low dissipation property and stability at large time step. For example, in many of the schemes [14, 17, 18, 20], the time step is limited by the relaxation time to get an accurate solution, even as the collision term is computed implicitly [17]. This drawback makes these OLB schemes very computational expensive when simulating high Reynolds number flows.

An alternative way to construct OLB schemes is to use the time-splitting strategy in solving the DVBE [1, 15, 16, 19, 21, 22], in which the DVBE is decomposed into a collision sub-equation and a followed pure advection sub-equation. The collision sub-equation is fully local and is discretized directly, leading to a collision step the same as the standard LBM; The collisionless advection subequation is then solved with certain numerical schemes on uniform or non-uniform meshes [15, 16], leading to a general streaming step. Specifically, the scheme proposed by Bardow et al., which combines the variable transformation technique for the collision term and the Lax-Wendroff scheme for the streaming step, overcomes the time step restriction by the relaxation time. It was demonstrated that accurate and stable solutions can be obtained even as the time step is much larger than the relaxation

time [1, 19, 23].

Recently, a finite volume kinetic scheme named discrete unified gas kinetic scheme (DUGKS) was proposed for all Knudsen number flows [2, 24]. In DUGKS the numerical flux is constructed based on the governing equation i.e., the DVBE itself, instead of using interpolations. With such a treatment, the time step is not restricted by the relaxation time, which is an indispensable property for effective continuum flow simulations. Its superior accuracy and stability for high Reynolds flows have been demonstrated [25]. In addition, it has been extended to arbitrary unstructured meshes recently [26].

Since both Bardow's scheme and DUGKS overcome the time step restriction from different approaches, it is still not clear the performance difference between them, so in this work we will present a comparative study of these two kinetic schemes for continuum flows, even though both of them are not limited to such flows. We will also investigate the link between the two schemes by comparing them in the same finite volume framework.

The remaining part of this paper is organized as follows. Sec. 2 will introduce DUGKS and Bardow's scheme and discuss their relation, Sec. 3 will present the comparison results, and a conclusion is given in Sec. 4.

2. Numerical formulation

2.1. Discrete Velocity Boltzmann-BGK equation

The governing equation Bardow's off-lattice Boltzmann schemes and DUGKS is the Boltzmann equation with the Bhatnagar-Gross-Krook collision operator [27],

$$\frac{\partial f}{\partial t} + \boldsymbol{\xi} \cdot \boldsymbol{\nabla} f = \Omega(f) \equiv \frac{f^{eq} - f}{\tau}, \tag{1}$$

where $f \equiv f(\boldsymbol{x}, \boldsymbol{\xi}, t)$ is the distribution function (DF) with particle velocity $\boldsymbol{\xi}$ at position $\boldsymbol{x}$ and time t, τ is relaxation time due to particle collisions, and f^{eq} is the Maxwellian equilibrium distribution function. In this article, we consider the isothermal two-dimensional-nine-velocities (D2Q9) lattice model. The corresponding DVBE is

$$\frac{\partial f_\alpha}{\partial t} + \boldsymbol{\xi}_\alpha \cdot \boldsymbol{\nabla} f_\alpha = \Omega(f_\alpha) \equiv \frac{f_\alpha^{eq} - f_\alpha}{\tau}, \tag{2}$$

where $f_\alpha \equiv f(\boldsymbol{x}, \boldsymbol{\xi}_\alpha, t)$ and $f_\alpha^{eq} \equiv f^{eq}(\boldsymbol{x}, \boldsymbol{\xi}_\alpha, t)$ are the DF with discrete velocity $\boldsymbol{\xi}_\alpha$ and the corresponding discrete equilibrium DF respectively. The D2Q9 discrete velocity set $\boldsymbol{\xi}_\alpha$ is given as

$$\boldsymbol{\xi}_\alpha = \begin{cases} (0,0) & \text{for } \alpha = 0, \\ \sqrt{3RT}\left(\cos[(\alpha-1)\pi/2], \sin[(\alpha-1)\pi/2]\right) & \text{for } \alpha = 1,2,3,4, \\ \sqrt{3RT}\left(\cos[(2\alpha-9)\pi/4], \sin[(2\alpha-9)\pi/4]\right)\sqrt{2} & \text{for } \alpha = 5,6,7,8, \end{cases} \tag{3}$$

3

where R is the gas constant and T is the constant temperature. Under the low Mach number condition, the discrete equilibrium DF can be approximated by its Taylor expansion around zero particle velocity up to second order, i.e.,

$$f_\alpha^{eq} = w_\alpha \rho \left[1 + \frac{\boldsymbol{\xi}_\alpha \cdot \boldsymbol{u}}{c_s^2} + \frac{(\boldsymbol{\xi}_\alpha \cdot \boldsymbol{u})^2}{2c_s^4} - \frac{|\boldsymbol{u}|^2}{2c_s^2} \right],$$ (4)

where $c_s = \sqrt{RT}$ is the lattice sound speed and the weights w_α are

$$w_\alpha = \begin{cases} 4/9 & \text{for } \alpha = 0, \\ 1/9 & \text{for } \alpha = 1, 2, 3, 4, \\ 1/36 & \text{for } \alpha = 5, 6, 7, 8. \end{cases}$$ (5)

The fluid density ρ and velocity $\boldsymbol{u}$ are the moments of discrete DFs,

$$\rho = \sum_\alpha f_\alpha, \quad \rho \boldsymbol{u} = \sum_\alpha \boldsymbol{\xi}_\alpha f_\alpha.$$ (6)

The shear viscosity of the fluid is related to the relaxation time by

$$\nu = \tau RT,$$ (7)

which can be deduced from Chapman-Enskog analysis [28]. The conservation property of the collision term is maintained at its discrete velocity counterpart, i.e.,

$$\sum_\alpha \Omega(f_\alpha) = 0, \quad \sum_\alpha \boldsymbol{\xi}_\alpha \Omega(f_\alpha) = 0.$$ (8)

2.2. Discrete unified gas kinetic scheme

The DUGKS employs a cell centered finite volume (FV) discretization of the DVBE [2]. The computational domain is firstly divided into small control volumes denoted by V_k. For a clear illustration of the formulas, we denote the volume averaged DF with discrete velocity ξ_α in control volume V_k at time level t^n by $f_{\alpha,k}^n$, i.e.,

$$f_{\alpha,k}^n = \frac{1}{|V_k|} \int_{V_k} f_\alpha(\boldsymbol{x}, t^n) dV.$$ (9)

It should be noted that the cell size should be fine enough to resolve the flow field and reduce the numerical errors [29, 30]. Then integrating Eq. (2) from time t^n to time t^{n+1} and applying the Gauss theorem we can get

$$f_{\alpha,k}^{n+1} - f_{\alpha,k}^n = -\frac{\Delta t}{|V_k|} \mathcal{F}_{\alpha,k,\text{dugks}} + \frac{\Delta t}{2} \left[\Omega(f_{\alpha,k}^n) + \Omega(f_{\alpha,k}^{n+1}) \right],$$ (10)

where $\mathcal{F}_{\alpha,k,\text{dugks}}$ is the numerical flux that flows into the control volume from its faces, and $\Delta t = t^{n+1} - t^n$ is the time step size. Note that trapezoidal rule is used for the collision term. This implicit

treatment of the collision term is crucial for its stability when the time step is much larger than the relaxation time. This implicitness can be removed in the actual implementation using the following variable transformation technique, which is also adopted by the standard LBM,

$$\tilde{f}_\alpha^n \equiv f_\alpha^n - \Delta t/2\Omega(f_\alpha^n), \quad \tilde{f}_\alpha^{+,n} \equiv f_\alpha^n + \Delta t/2\Omega(f_\alpha^n). \tag{11}$$

Equation (10) can be now rewritten in an explicit form,

$$\tilde{f}_{\alpha,k}^{n+1} = \tilde{f}_{\alpha,k}^{n,+} - \frac{\Delta t}{|V_k|}\mathcal{F}_{\alpha,k,\text{dugks}}. \tag{12}$$

In the implementation, we track the evolution of $\tilde{f}_{\alpha,k}$ instead of the original DFs. At the beginning of each time step, $\tilde{f}_{\alpha,k}^{+,n}$ can be obtained from $\tilde{f}_{\alpha,k}^n$ according to Eq. (11) [2],

$$\tilde{f}_{\alpha,k}^{+,n} = \frac{2\tau - \Delta t}{2\tau + \Delta t}\tilde{f}_{\alpha,k}^n + \frac{2\Delta t}{2\tau + \Delta t}f_{\alpha,k}^{eq,n} \tag{13}$$

where the macroscopic variables used to evaluate the equilibrium DF $f^{eq,n}$ can be calculated from the transformed DF $\tilde{f}$ due to the conservation property of the collision term, i.e.,

$$\rho^n = \sum_\alpha \tilde{f}_\alpha^n, \quad \rho^n \boldsymbol{u}^n = \sum_\alpha \boldsymbol{\xi}_\alpha \tilde{f}_\alpha^n. \tag{14}$$

The key merit of DUGKS lies in its treatment of the advection term, i.e., the way to construct the numerical flux $\mathcal{F}_{\alpha,k,\text{dugks}}$. In DUGKS, the middle point rule is used for the integration of the flux over the time step,

$$\mathcal{F}_{\alpha,k,\text{dugks}} = \int_{\partial V_k} (\boldsymbol{\xi}_\alpha \cdot \boldsymbol{n}) f_{\alpha,\text{dugks}}^{n+1/2} dS. \tag{15}$$

The integration over the cell faces is computed by the $f_\alpha^{n+1/2}$ at the centers of the cell faces, which themselves are computed using the characteristic solution of the kinetic equation (2). Supposing the center of a face is $\boldsymbol{x}_b$, then by integrating Eq. (2) along the characteristic line in a half time step $h = \Delta t/2$ from $(t^n, \boldsymbol{x}_b - h\boldsymbol{\xi}_\alpha)$ to $(t^{n+1/2}, \boldsymbol{x}_b)$, and applying the trapezoidal rule, we can get

$$f_{\alpha,\text{dugks}}^{n+1/2}(\boldsymbol{x}_b) - f_\alpha^n(\boldsymbol{x}_b - h\boldsymbol{\xi}_\alpha) = \frac{h}{2}\left[\Omega(f_\alpha^n(\boldsymbol{x}_b)) + \Omega\left(f_\alpha^{n+1/2}(\boldsymbol{x}_b - h\boldsymbol{\xi}_\alpha)\right)\right]. \tag{16}$$

Again the implicitness can be eliminated by introducing another two variable transformations,

$$\bar{f}_\alpha^{n+1/2}(\boldsymbol{x}_b) \equiv f_\alpha^{n+1/2}(\boldsymbol{x}_b) - \frac{h}{2}\Omega\left(f_\alpha^{n+1/2}(\boldsymbol{x}_b)\right), \quad \bar{f}_\alpha^{+,n}(\boldsymbol{x}_b - h\boldsymbol{\xi}_\alpha) \equiv f_\alpha^n(\boldsymbol{x}_b - h\boldsymbol{\xi}_\alpha) + \frac{h}{2}\Omega\left(f_\alpha^n(\boldsymbol{x}_b - h\boldsymbol{\xi}_\alpha)\right). \tag{17}$$

Then we can reformulate Eq. (16) in the following explicit form,

$$\bar{f}_\alpha^{n+1/2}(\boldsymbol{x}_b) = \bar{f}_\alpha^{n,+}(\boldsymbol{x}_b - h\boldsymbol{\xi}_\alpha). \tag{18}$$

For smooth i.e., well-resolved shock-free flows, $\bar{f}_\alpha^{+,n}(\boldsymbol{x}_b - h\boldsymbol{\xi})$ can be interpolated linearly from $\bar{f}_\alpha^{+,n}$ at its neighboring cell centers which themselves can be calculated from the tracked $\tilde{f}_\alpha^n$ similar to Eq. (13),

$$\bar{f}_\alpha^{+,n} = \frac{2\tau - h}{2\tau + \Delta t}\tilde{f}_\alpha^n + \frac{3h}{2\tau + \Delta t}f_\alpha^{eq,n}. \tag{19}$$

The details of the linear interpolation will be further given later. It should be noted that, when discontinuities such as shock wave are involved, more sophisticated advection schemes such as upwind schemes with slope/flux limiters [24, 26, 31], flux splitting schemes [20, 32] and even weighted essentially non-oscillatory (WENO) schemes [33] should be employed in order to obtain stable solutions.

After getting $\bar{f}_\alpha^{n+1/2}(\boldsymbol{x}_b)$, the original DF $f_\alpha^{n+1/2}(\boldsymbol{x}_b)$ can be transformed back with the help of Eq. (17) as,

$$f_\alpha^{n+1/2} = \frac{2\tau}{2\tau + h}\bar{f}_\alpha^{n+1/2} + \frac{h}{2\tau + h}f_\alpha^{eq,n+1/2}. \tag{20}$$

The macroscopic fluid variable $\rho^{n+1/2}(\boldsymbol{x}_b)$ and $\boldsymbol{u}^{n+1/2}(\boldsymbol{x}_b)$ used in $f^{eq,n+1/2}$ are calculated from,

$$\rho^{n+1/2}\Big|_{\boldsymbol{x}_b} = \sum_\alpha \bar{f}_\alpha^{n+1/2}(\boldsymbol{x}_b), \quad (\rho\boldsymbol{u})^{n+1/2}\Big|_{\boldsymbol{x}_b} = \sum_\alpha \boldsymbol{\xi}_\alpha \bar{f}_\alpha^{n+1/2}(\boldsymbol{x}_b). \tag{21}$$

To insure the interpolation in Eq. (18) is stable, the time step is limited by the CFL condition,

$$\Delta t = \eta \frac{\Delta x}{|\boldsymbol{\xi}|_{\max}} = \eta \frac{\Delta x}{\sqrt{6}c_s}, \tag{22}$$

where $0 < \eta < 1$ is the CFL number and Δx measures the size of the cell.

For completeness, the step-by-step algorithm of DUGKS is outlined as follows [2, 24]:

1. At the beginning ($n = 0$), the fluid variables (ρ^0 and $\boldsymbol{u}^0$) and the transformed DFs $\tilde{f}_\alpha^0$ at each cell center are initialised.

2. $\tilde{f}_\alpha^{+,n}$ and $\bar{f}_\alpha^{+,n}$ at each cell center are calculated using Eqs. (13) and (19), respectively.

3. $\bar{f}_\alpha^{n+1/2}$ at each cell interface is obtained by shifting the upwind $\bar{f}_\alpha^{+,n}$ which is interpolated from nearby cell centers.

4. At each cell interface, $\rho^{n+1/2}$ and $\boldsymbol{u}^{n+1/2}$ are calculated from $\bar{f}^{n+1/2}$ using Eq. (21).

5. The original DF at each cell interface $f_\alpha^{n+1/2}$ is transformed back according to Eq. (20).

6. At each cell center, $\tilde{f}_\alpha^{n+1}$ is updated from $\tilde{f}_\alpha^{+,n}$ at the cell center and $f_\alpha^{n+1/2}$ at the surrounding cell interfaces using Eq. (12) and Eq. (15).

7. ρ^{n+1} and $\boldsymbol{u}^{n+1}$ at each cell center are calculated from $\tilde{f}_\alpha^{n+1}$ using Eq. (14).

8. Advance the time step ($n \leftarrow n + 1$) and repeat step 2 to 8 until the end.

2.3. Bardow's off-lattice Boltzmann scheme

Bardow's off-lattice Boltzmann scheme is based on a characteristic discretization of the DVBE. Integrating Eq. (1) along the characteristics from t^n to t^{n+1} and approximated the collision term by the Crank-Nicolson (trapezoidal) rule gives [1],

$$\check{f}_\alpha^{n+1} = \check{f}_\alpha^n + \frac{\Delta t}{2} \left[\check{\Omega}_\alpha^n + \check{\Omega}_\alpha^{n+1} \right]. \tag{23}$$

The check symbol (˘) denotes a variable on the characteristics with a velocity of $\boldsymbol{\xi}_\alpha$. For example, $\check{f}_\alpha^n = f_\alpha(\boldsymbol{x}, t^n)$ and $\check{f}_\alpha^{n+1} = f_\alpha(\boldsymbol{x} + \boldsymbol{\xi}_\alpha \Delta t, t^{n+1})$. Note that other integrating rules for the collision term have also been discussed in Bardow's work [1]. By introducing the following function [1],

$$g_\alpha(\boldsymbol{x}, t) = f_\alpha(\boldsymbol{x}, t) - \frac{\Delta t}{2} \Omega_\alpha \left(f(\boldsymbol{x}, t) \right), \tag{24}$$

and employing the property of $g^{eq} = f^{eq}$, Eq. (23) can be rewritten as [1]

$$\check{g}_\alpha^{n+1} = \check{g}_\alpha^n - \frac{\Delta t}{\lambda} (\check{g}_\alpha^n - \check{g}_\alpha^{eq,n}), \tag{25}$$

where $\lambda = \tau + 1/2\Delta t$. Applying the characteristic solution and second order Taylor expansions to the RHS of the Eq. (25), Bardow et al. obtained the following general updating rule of their off-lattice Boltzmann schemes [1],

$$\begin{aligned} g_\alpha^{n+1} = g_\alpha^n - \Delta t \left[\xi_{\alpha i} \frac{\partial g_\alpha^n}{\partial x_i} + \frac{1}{\lambda} (g_\alpha^n - g_\alpha^{eq,n}) \right] \\ + \frac{\Delta t^2}{2} \xi_{\alpha i} \frac{\partial}{\partial x_i} \left[\xi_{\alpha j} \frac{\partial g_\alpha^n}{\partial x_j} + \frac{2}{\lambda} (g_\alpha^n - g_\alpha^{eq,n}) \right] + \frac{\Delta t^3}{2\lambda} \xi_{\alpha i} \frac{\partial}{\partial x_i} \left[\xi_{\alpha j} \frac{\partial (g_\alpha^n - g_\alpha^{eq,n})}{\partial x_j} \right], \end{aligned} \tag{26}$$

where the subscripts $i, j = 1, 2$ denote the spatial indices and summations are taken over repeated i and j. Equation (26) may look complicated at first glance, but it can be simplified to the following form if we notice the equivalence between g_α and $\tilde{f}_\alpha$, and $\tilde{f}^+ = g - (\Delta t/\lambda)(g_\alpha - g_\alpha^{eq})$ (see Eq. (11) and Eq. (24)),

$$\tilde{f}_\alpha^{n+1} = \tilde{f}_\alpha^{+,n} - \Delta t \xi_{\alpha i} \frac{\partial \tilde{f}_\alpha^{+,n}}{\partial x_i} + \frac{\Delta t^2}{2} \xi_{\alpha i} \xi_{\alpha j} \frac{\partial^2 \tilde{f}_\alpha^{+,n}}{\partial x_i \partial x_j}, \tag{27}$$

which Eq. (27) share similarities with the collision-streaming algorithm in the standard LBM. At the beginning of each time step, $\tilde{f}_\alpha^+$ is calculated from $\tilde{f}_\alpha$ through

$$\tilde{f}_\alpha^+ = \tilde{f}_\alpha - (\Delta t/\lambda)(\tilde{f}_\alpha - \tilde{f}_\alpha^{eq}) = \frac{2\tau - \Delta t}{2\tau + \Delta t} \tilde{f}^n + \frac{2\Delta t}{2\tau + \Delta t} f^{eq,n}, \tag{28}$$

which is the same as the DUGKS and is also the collision step in the standard LBM method. Then the pure advection equation is solved to update $\tilde{f}_\alpha$. The difference is that the standard LBM solves the pure advection equation exactly through shifts of the post-collision DF between neighboring nodes in the streaming process, while Bardow's scheme solves it using the Lax-Wendroff scheme [34]. It should

also be mentioned that if we apply the one dimensional Lax-Wendroff scheme to solve the advection equation in each discrete velocity direction on a uniform Cartesian grid, Bardow's scheme reduces to the scheme developed in Ref. [21].

In the original works [1, 19], either finite element (FE) or finite difference (FD) is employed to further discretize the spatial gradients in Eq. (27). In a two dimensional FD implementation of Bardow's scheme [23], the central finite difference schemes on a uniform mesh are used, i.e., the first and second order spatial derivatives in Eq. (26) are computed as [23],

$$\frac{\partial \tilde{f}_\alpha^{+,n}}{\partial x_1}\bigg|_{l,m} = \frac{\tilde{f}_{\alpha,l+1,m}^{+,n} - \tilde{f}_{\alpha,l-1,m}^{+,n}}{2\Delta x_1}, \tag{29a}$$

$$\frac{\partial \tilde{f}_\alpha^{+,n}}{\partial x_2}\bigg|_{l,m} = \frac{\tilde{f}_{\alpha,l,m+1}^{+,n} - \tilde{f}_{\alpha,l,m-1}^{+,n}}{2\Delta x_2}, \tag{29b}$$

$$\frac{\partial^2 \tilde{f}_\alpha^{+,n}}{\partial x_1^2}\bigg|_{l,m} = \frac{\tilde{f}_{\alpha,l+1,m}^{+,n} + \tilde{f}_{\alpha,l-1,m}^{+,n} - 2\tilde{f}_{\alpha,l,m}^{+,n}}{\Delta x_1^2}, \tag{29c}$$

$$\frac{\partial^2 \tilde{f}_\alpha^{+,n}}{\partial x_2^2}\bigg|_{l,m} = \frac{\tilde{f}_{\alpha,l,m+1}^{+,n} + \tilde{f}_{\alpha,l,m-1}^{+,n} - 2\tilde{f}_{\alpha,l,m}^{+,n}}{\Delta x_2^2}, \tag{29d}$$

$$\frac{\partial^2 \tilde{f}_\alpha^{+,n}}{\partial x_1 \partial x_2}\bigg|_{l,m} = \frac{1}{4\Delta x_1 \Delta x_2}[\tilde{f}_{\alpha,l+1,m+1}^{+,n} - \tilde{f}_{\alpha,l-1,m+1}^{+,n} - \tilde{f}_{\alpha,l+1,m-1}^{+,n} + \tilde{f}_{\alpha,l-1,m-1}^{+,n}], \tag{29e}$$

where the computational stencil for each node is illustrated in Fig. 1. It should be noted that the central schemes for the biased derivatives (both ∂ and ∂^2) are not isotropic [35]. For problems with microstructure evolution where physical anisotropy is important, such as crystal growth and multiphase flows, isotropic finite difference schemes are preferred as they introduce less numerical anisotropy into simulations [35]. Actually in multiphase LBM models, derivatives and Laplacian are often discretized using isotropic finite difference schemes [28].

In the following, we will illustrate a two dimensional FV discretization of Eq. (27) similar to the DUGKS and demonstrate its equivalence to the FD implementation using Eq. (29). Firstly, divide the computation domain into cells by line segments (cell interfaces) that cross the centers of links between FD nodes (see Fig.1). The index of each cell is the same as the index of the FD node it encloses. Then rewrite Eq. (27) as,

$$\tilde{f}_\alpha^{n+1} = \tilde{f}_\alpha^{+,n} - \Delta t \xi_{\alpha i} \frac{\partial}{\partial x_i}\left[\tilde{f}_\alpha^{+,n} - \frac{\Delta t}{2}\xi_{\alpha j}\frac{\partial \tilde{f}_\alpha^{+,n}}{\partial x_j}\right]. \tag{30}$$

Integrating it in each cell gives

$$\tilde{f}_{\alpha,l,m}^{n+1} = \tilde{f}_{\alpha,l,m}^{+,n} - \frac{\Delta t}{|V_{l,m}|}\int_{\partial V_{l,m}}(\boldsymbol{\xi}_\alpha \cdot \boldsymbol{n})\left[\tilde{f}_\alpha^{+,n} - \frac{\Delta t}{2}\xi_{\alpha j}\frac{\partial \tilde{f}_\alpha^{+,n}}{\partial x_j}\right]\mathrm{d}S \tag{31}$$

where $|V_{l,m}|$ is the volume of cell (l,m) and $\tilde{f}_{\alpha,l,m}$ and $\tilde{f}_{\alpha,l,m}^+$ are cell-averaged DFs, $\boldsymbol{n}$ is the unit normal vector of the cell interface pointing outside. Note that similar to Eq. (12), we can also represent the
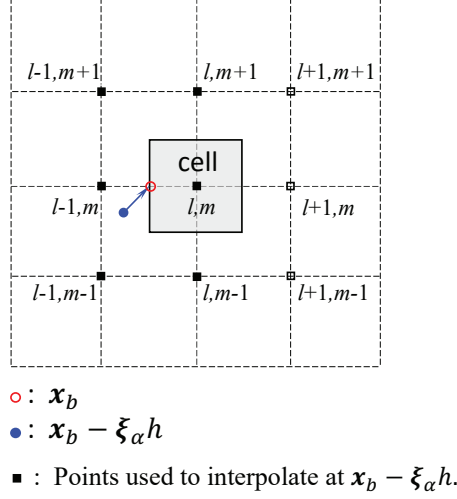
Figure 1: Illustration of the finite volume discretization and the interpolation scheme.

FV updating rule as

$$\tilde{f}_{\alpha,l,m}^{n+1} = \tilde{f}_{\alpha,l,m}^{n,+} - \frac{\Delta t}{|V_{l,m}|}\mathcal{F}_{\alpha,l,m,\text{Bardow}}, \tag{32}$$

where the time integration is approximated using the middle point rule, i.e.,

$$\mathcal{F}_{\alpha,l,m,\text{Bardow}} = \int_{\partial V_{l,m}} (\boldsymbol{\xi}_\alpha \cdot \boldsymbol{n}) f_{\alpha,\text{Bardow}}^{n+1/2} \mathrm{d}S. \tag{33}$$

From Eq. (31) to (33), the following equation can be easily deduced,

$$f_{\alpha,\text{Bardow}}^{n+1/2}(\boldsymbol{x}_b) = \tilde{f}_\alpha^{+,n}(\boldsymbol{x}_b) - \frac{\Delta t}{2}\xi_{\alpha j}\frac{\partial \tilde{f}_\alpha^{+,n}(\boldsymbol{x}_b)}{\partial x_j}, \tag{34}$$

where $\boldsymbol{x}_b$ is the center of cell interface and the middle point rule is employed in the integration of Eq. (33). The RHS of Eq. (34) is a first order Taylor expansion of $\tilde{f}^+$ around $\boldsymbol{x}_b$ in the direction of $\boldsymbol{\xi}_\alpha$, therefore it is an approximation of the following equation,

$$f_{\alpha,\text{Bardow}}^{n+1/2}(\boldsymbol{x}_b) = \tilde{f}_\alpha^{+,n}(\boldsymbol{x}_b - h\boldsymbol{\xi}_\alpha) = f_\alpha^n(\boldsymbol{x}_b - h\boldsymbol{\xi}_\alpha) + h\Omega\left(f_\alpha^n(\boldsymbol{x}_b - h\boldsymbol{\xi}_\alpha)\right). \tag{35}$$

where $h = \Delta t/2$. This equation will be further compared with Eq. (16) next.

It can be found that the updating procedures of this FV version of the Bardow's scheme is similar to DUGKS and is simpler because $f_\alpha^{n+1/2}(\boldsymbol{x}_b)$ is directly interpolated from $\tilde{f}_\alpha^+$ from the upwind in this scheme. Note that the interpolation scheme needs to be specified in both DUGKS and this scheme in order to get $\tilde{f}_\alpha^+(\boldsymbol{x}_b - h\boldsymbol{\xi}_\alpha)$ or $\bar{f}_\alpha^+(\boldsymbol{x}_b - h\boldsymbol{\xi}_\alpha)$ (see Eq. (18) and Eq. (35)). In the following, we only describe the interpolation scheme used in this FV version of Bardow's scheme and the same approach is also adopted in the implementation of DUGKS in this work. On quadrilateral structured grids, the FV based Bardow's scheme can be formulated as

$$\tilde{f}_{\alpha,l,m}^{n+1} = \tilde{f}_{\alpha,l,m}^{+,n} - \frac{\xi_{\alpha 1}\Delta t}{\Delta x_1}\left[f_{\alpha,l+1/2,m}^{n+1/2} - f_{\alpha,l-1/2,m}^{n+1/2}\right] - \frac{\xi_{\alpha 2}\Delta t}{\Delta x_2}\left[f_{\alpha,l,m+1/2}^{n+1/2} - f_{\alpha,l,m-1/2}^{n+1/2}\right], \tag{36}$$

9

where $f_{\alpha,l\pm1/2,m}^{n+1/2}$ and $f_{\alpha,l,m\pm1/2}^{n+1/2}$ are DFs at the face centers of cell (l,m) at the half time step, which have to be interpolated from the upwind using $\tilde{f}_\alpha^n$ at the neighboring cell centers. Taking $f_{\alpha,l-1/2,m}^{n+1/2}$ for example, as illustrated in Fig. 1, it can be interpolated bilinearly from the upwind using the six neighboring cell centers with the following formula,

$$
\begin{aligned}
f_{\alpha,l-1/2,m}^{n+1/2} &= \frac{1}{2}[\tilde{f}_{\alpha,l,m}^{+,n} + \tilde{f}_{\alpha,l-1,m}^{+,n}] - \frac{\xi_{\alpha1}\Delta t}{2\Delta x_1}[\tilde{f}_{\alpha,l,m}^{+,n} - \tilde{f}_{\alpha,l-1,m}^{+,n}] \\
&\quad - \frac{\xi_{\alpha2}\Delta t}{8\Delta x_2}[\tilde{f}_{\alpha,l-1,m+1}^{+,n} + \tilde{f}_{\alpha,l,m+1}^{+,n} - \tilde{f}_{\alpha,l-1,m-1}^{+,n} - \tilde{f}_{\alpha,l,m-1}^{+,n}].
\end{aligned}
\tag{37}
$$

The remaining $f_\alpha^{n+1/2}$ in Eq. (36) can be calculated similarly. Then one can immediately check the equivalence between Eq. (36) and Eq. (27) subjected to the difference schemes in Eq. (29), which means the current FV based Bardow's scheme is equivalent to the original FD based implementation. It should be noted that, the above presentations are based on spatial discretization using uniform Cartesian mesh. However, for non-uniform Cartesian meshes, such equivalence can also be verified. We also note that by discretizing Eq. (27) using the FV approach, Bardow's scheme can also be extended to general unstructured meshes just like DUGKS [26].

As a summary, the step-by step algorithm of the FV implementation of Bardow's scheme is outlined as follows:

1. At the beginning $(n = 0)$, the fluid variables $(\rho^0$ and $\boldsymbol{u}^0)$ and the transformed distribution functions $\tilde{f}_\alpha^0$ at each cell center are initialised.

2. $\tilde{f}_\alpha^{+,n}$ at each cell center is calculated using Eq. (28).

3. $f_\alpha^{n+1/2}$ at each cell interface is obtained by shifting the upwind $\tilde{f}_\alpha^{+,n}$ which is interpolated from nearby cell centers like the example expressed in Eq. (37).

4. At each cell center, $\tilde{f}_\alpha^{n+1}$ is updated from $\tilde{f}_\alpha^{+,n}$ at the cell center and $f_\alpha^{n+1/2}$ at the surrounding cell interfaces using Eq. (32) and the definition in Eq. (33).

5. ρ^{n+1} and $\boldsymbol{u}^{n+1}$ at each cell center are calculated from $\tilde{f}_\alpha^{n+1}$ using Eq. (14).

6. Advance the time step $(n \leftarrow n + 1)$ and repeat steps 2 to 6 until end time or steady state is reached.

2.4. Comparison of the numerical fluxes in DUGKS and Bardow's scheme

We now analyses the differences between DUGKS and Bardow's scheme in finite-volume framework. This is achieved by analyzing accuracy of the reconstructed distribution function at the cell interface center. Firstly, it is noted that the exact solution of the DVBE at the cell interface center at middle time step is

$$
f_{\alpha,\text{exact}}^{n+1/2}(\boldsymbol{x}_b) = f_\alpha^n(\boldsymbol{x}_b - h\boldsymbol{\xi}_\alpha) + \int_0^h \Omega\left(f_\alpha(\boldsymbol{x}_b - h\boldsymbol{\xi}_\alpha + s\boldsymbol{\xi}_\alpha, t^n + s)\right) ds.
\tag{38}
$$

10

We can immediately find that if we approximate the integration of the collision term in Eq. (38) using the rectangular integrating rule, i.e., the integration term is approximated as $h\Omega(f(\boldsymbol{x}_b - h\boldsymbol{\xi}_\alpha))$, we get Eq. (35), which is the flux formula in Bardow's scheme. On the other hand, if we apply the trapezoidal rule to the quadrature, we get Eq. (16), i.e., the flux formula in DUGKS. Thus, in both DUGKS and Bardow's scheme, the flux is determined from the local characteristic solution of the DVBE. The convection and collision effects are considered simultaneously in the evaluation of the distribution function flux.

The using of the local solution of the governing equation to compute the numerical flux in DUGKS and Bardow's scheme is conceptually different from the pure mathematic treatments of the advection term in many other FV/FD off-lattice Boltzmann schemes [14, 13, 36, 17, 31, 20, 37, 32]. Often in these schemes, special care has to be taken to stabilize the computation as well as minimize the numerical dissipation, even though advanced CFD technique such as limiters [31] or total variation diminishing (TDV) [20, 32] are employed.

First it is noted that the reconstructed distribution function at a cell interface in DUGKS and Bardow's scheme in Eqs. (16) and (35) can also be rewritten as

$$
\begin{aligned}
f_{\alpha,\text{dugks}}^{n+1/2}(\boldsymbol{x}_b) &= f_\alpha^n(\boldsymbol{x}_b - h\boldsymbol{\xi}_\alpha) + \frac{h}{2}\left[\Omega\left(f_\alpha^n(\boldsymbol{x}_b - h\boldsymbol{\xi}_\alpha)\right) + \Omega(f_\alpha^{n+1/2}(\boldsymbol{x}_b))\right] \\
&= f_{\alpha,\text{exact}}^{n+1/2}(\boldsymbol{x}_b) + O(\Delta x^m) + \frac{h^3}{12}D_\alpha^2\Omega(f^n(\boldsymbol{x}_b)) + O(h^4), \quad (39a)
\end{aligned}
$$

$$
\begin{aligned}
f_{\alpha,\text{Bardow}}^{n+1/2}(\boldsymbol{x}_b) &= f_\alpha^n(\boldsymbol{x}_b - h\boldsymbol{\xi}_\alpha) + h\Omega\left(f_\alpha^n(\boldsymbol{x}_b - h\boldsymbol{\xi}_\alpha)\right) \\
&= f_{\alpha,\text{exact}}^{n+1/2}(\boldsymbol{x}_b) + O(\Delta x^m) - \frac{h^2}{2}D_\alpha\Omega(f_\alpha^n(\boldsymbol{x}_b)) + O(h^3), \quad (39b)
\end{aligned}
$$

where $D_\alpha \equiv \partial_t + \boldsymbol{\xi}_\alpha \cdot \boldsymbol{\nabla}$. The error terms $O(\Delta x^m)$ come from the spatial interpolation. For the currently implemented linear interpolation, $m = 2$. The leading errors introduced by approximating the integration of the collision term in Eq. (38) are explicitly expressed in Eq. (39a) and Eq. (39b) for the two schemes, i.e, $E_{\text{dugks}} = (h^3/12)D_\alpha^2\Omega = O(h^3)$ and $E_{\text{Bardow}} = -(h^2/2)D_\alpha\Omega = O(h^2)$, which means DUGKS is more accurate than Bardow's scheme in general. Particularly, for flows near a wall, the orders of magnitude of the two error terms can be estimated as

$$
E_{\text{dugks}} \sim h\frac{h^2}{\delta^2} \sim h\left(\frac{\eta\Delta x}{\delta}\right)^2 \quad (40a)
$$

$$
E_{\text{Bardow}} \sim h\frac{h}{\delta} \sim h\frac{\eta\Delta x}{\delta}, \quad (40b)
$$

where $\delta \sim L/\sqrt{\text{Re}}$ is characteristic thickness of the boundary layer [50] with L being the characteristic length and Re the typical Reynolds number. Generally, within the boundary layer several grid nodes are required in order to capture the flow dynamics correctly, meaning that $\eta\Delta x/\delta < 1$. Therefore, two

conclusions can be inferred immediately from the above estimations, namely, (i) Simulation errors near a solid wall will increase with increasing Reynolds number for both DUGKS and Bardow's scheme, but DUGKS will be more accurate; (ii) DUGKS will be less sensitive to mesh size than Bardow's scheme for flows involving solid walls. We here also argue that, as DUGKS employs an implicit treatment of the collision term in the evaluation of numerical flux, it is expected to be more stable than Bardow's scheme. These arguments are also confirmed in the later numerical simulations.

We shall remark that if the distribution functions at cell interfaces are obtained by direct linear interpolation along the characteristic line, i.e., neglecting the integral of the collision term in Eq. (38), the numerical flux can be represented as

$$
\begin{aligned}
f_{\alpha,\text{FT}}^{n+1/2}(\boldsymbol{x}_b) &= f_\alpha^n(\boldsymbol{x} - h\boldsymbol{\xi}) + O(\Delta x^2) \\
&= f_\alpha^{(0),n}(\boldsymbol{x}_b - h\boldsymbol{\xi}_\alpha) + \tau f^{(1),n}(\boldsymbol{x}_b - h\boldsymbol{\xi}_\alpha) + O(\Delta x^2) + O(\tau^2),
\end{aligned}
\tag{41}
$$

where the subscript FT means the free transport (without collision) and the Chapman-Enskog expansion [28], i.e, $f_\alpha = f_\alpha^{(0)} + \tau f_\alpha^{(1)} + O(\tau^2)$ has been used. While, the exact flux expression in Eq. (38) can be expanded as

$$
\begin{aligned}
f_{\alpha,\text{exact}}^{n+1/2}(\boldsymbol{x}_b) &= f_\alpha^{(0),n}(\boldsymbol{x}_b - h\boldsymbol{\xi}_\alpha) + \tau f^{(1),n}(\boldsymbol{x}_b - h\boldsymbol{\xi}_\alpha) + \int_0^h \Omega_\alpha(\boldsymbol{x}_b - h\boldsymbol{\xi}_\alpha + \boldsymbol{\xi}_\alpha s, s)ds + O(\tau^2) \\
&= f_\alpha^{(0),n}(\boldsymbol{x}_b - h\boldsymbol{\xi}_\alpha) + (\tau - h)f^{(1),n}(\boldsymbol{x}_b - h\boldsymbol{\xi}_\alpha) + O(\tau h) + O(\tau^2)
\end{aligned}
\tag{42}
$$

Comparing Eq. (41) with the exact distribution function given by Eq. (42), we can see the missing term is $-hf_\alpha^{(1),n}(\boldsymbol{x}_b - h\boldsymbol{\xi}_\alpha)$. As the second order moment of $f^{(1),n}$ in the velocity space contributes directly to the diffusive flux, the lack of the collision term in the reconstruction of cell-interface distribution function is equivalent to introduce a numerical viscosity proportional to Δt [38, 39, 40, 41].

2.5. No-slip boundary condition

In this subsection, we briefly mention the implementation of no-slip boundary condition for Bardow's scheme and DUGKS. The basic idea here is to mimic the half-way bounce-back rule of the standard LBM [28] by reversing the DFs at boundary faces at middle time steps. Fig. 2 illustrates a vertical boundary face located at a no slip wall with velocity $\boldsymbol{U}_\text{w}$. Both of the incoming and outgoing DFs at the boundary face at middle time steps have to be provided to update the cell-centered DFs. We denote the incoming and outgoing DFs by $\hat{\phi}_{\text{w},j,\text{in}}^{n+1/2}$ and $\hat{\phi}_{\text{w},j,\text{out}}^{n+1/2}$ respectively, where $\hat{\phi}_{\text{w},j}^{n+1/2}$ stands for $\bar{f}_{\text{w},j}^{n+1/2}$ in DUGKS and $f_{\text{w},j}^{n+1/2}$ in Bardow's scheme. The ghost cell method is used to facilitate the implementation of the no-slip boundary condition. An extra layer of cells (ghost cells) are allocated outside of the wall. The unknown DFs $\phi_{0,j}^n$ in the ghost cells are extrapolated linearly from the values on their neighboring inner cell centers, i.e., $\phi_{1,j}$ and $\phi_{2,j}$. Here, ϕ^n stands for $\bar{f}^{+,n}$ and $\tilde{f}^{+,n}$ in DUGKS
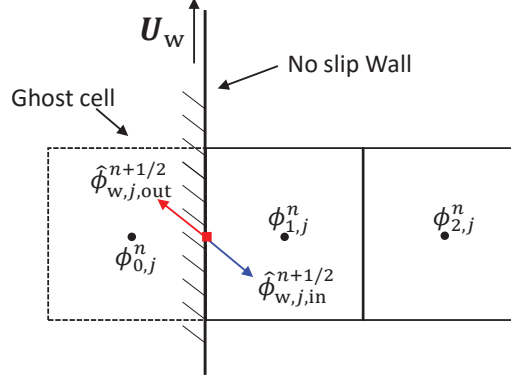
Figure 2: Diagrammatic sketch of the implementation of no-slip wall boundary condition.

and Bardow's scheme, respectively. Then we can compute the $\hat{\phi}_{\text{w,j,out}}^{n+1/2}$ normally like the internal cell interfaces. Finally, the incoming DFs are calculated in the same way as the half-way bounce-back rule in the standard LBM [28],

$$\hat{\phi}_{\text{w,j},\bar{\alpha}}^{n+1/2} = \hat{\phi}_{\text{w,j},\alpha}^{n+1/2} - 2w_\alpha \rho_{\text{w},j} \frac{\boldsymbol{\xi}_\alpha \cdot \boldsymbol{U}_{\text{w}}}{c_s^2}, \tag{43}$$

where α stands for an outgoing DF direction and $\bar{\alpha}$ is its reverse direction. $\rho_{\text{w},j}$ is extrapolated from the nearest neighbour cell, i.e., $\rho_{\text{w},j} = \rho_{1,j}$.

The above implementation for the no-slip boundary condition in DUGKS has been previously adopted in Refs. [25] and [42], and has been demonstrated to be second order accurate [42]. Here for the Bardow's scheme, we also use a numerical test to verify its second order accuracy subjected to such kind of implementation for non-slip walls. The test case is the steady state force-driven general Couette flow between parallel plates. The plates are placed horizontally between $0 < y < L$, where the bottom plate is kept fixed while the top one moves to the right with a constant velocity U_{w}. The inlet and outlet of the channel are assumed to be periodical. A constant horizontal body force ρG is exerted on the fluid. The analytical horizontal velocity profile at steady state is given by,

$$u_a(y) = \frac{y}{L} U_{\text{w}} + \frac{G}{\nu} \frac{L^2}{2} \left(\frac{y}{L} - \frac{y^2}{L^2} \right). \tag{44}$$

In simulations, we set $L = 1$ and $U_{\text{w}} = 0.05$, while the grid number across the channel (N_y) is varied. The CFL number is set to be 0.5. The collision time is fixed at $\tau = 0.5\Delta t$. The body force G is adjusted to keep the maximum velocity at $u_a(y)|_{\max} = 0.1$. The discrete body force scheme of He et. al. [43] is applied in the same way as in the standard LBM. The relative L_2 errors of the simulated velocity $u_n(y)$ defined as

$$E_u = \frac{\sqrt{\sum_y |\boldsymbol{u}_n(y) - \boldsymbol{u}_a(y)|^2}}{\sqrt{\sum_y |\boldsymbol{u}_a(y)|^2}}, \tag{45}$$
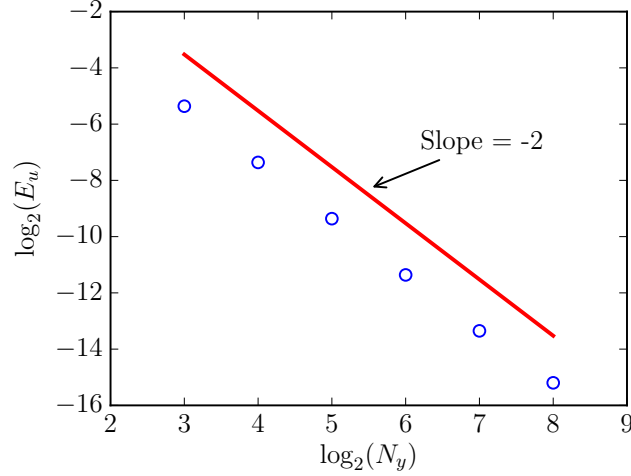
13

Figure 3: L_2 error (blue circle) of the velocity profile as a function of the mesh size (N_y) for the general Couette flow predicted by Bardow's scheme.

are calculated under different N_y. The results are presented in Fig. 3. It can be seen that the current implementation of the no-slip boundary condition in Bardow's scheme achieves a second order accuracy.

3. Numerical tests

In this section, we compare DUGKS and Bardow's scheme in terms of accuracy, stability and computational efficiency by simulating several two dimensional flows. The first one is the unsteady Taylor-Green vortex flow which is free from boundary effect, and an analytical solution exists for this problem. The second test case is the lid-driven cavity flow, which is used to evaluate the accuracy and stability, and the last one is the laminar boundary layer flow problem, which is used to verify the dissipation property of DUGKS and Bardow's scheme. In all of our simulations, the CFL number is set to be 0.5 and the criterion for reaching steady state in the simulations is

$$\frac{\sqrt{\sum_{l,m}|\boldsymbol{u}_{l,m}^{n}-\boldsymbol{u}_{l,m}^{n-1000}|^2}}{\sqrt{\sum_{l,m}|\boldsymbol{u}_{l,m}^{n-1000}|^2}} < 10^{-8},\tag{46}$$

unless stated otherwise.

3.1. Taylor-Green vortex flow

This problem is a two dimensional unsteady incompressible flow in a square domain with periodical condition in both directions. The analytical solution is given by

$$u(x, y, t) = -U_0 \cos(2\pi x) \sin(2\pi y) \exp(-8\pi^2 \nu t), \tag{47a}$$

$$v(x, y, t) = U_0 \sin(2\pi x) \cos(2\pi y) \exp(-8\pi^2 \nu t), \tag{47b}$$

$$p(x, y, t) = -\frac{U_0^2}{4} \left[\cos(4\pi x) + \cos(4\pi y)\right] \exp(-16\pi^2 \nu t), \tag{47c}$$

where U_0 is a constant indicating the velocity magnitude and hence the kinetic energy of the initial flow field, ν is the shear viscosity, $\boldsymbol{u} = (u, v)$ is the velocity, and p is the pressure. The computation domain is $0 < x < L$ and $0 < y < L$ with $L = 1$. We set $U_0 = 1/\sqrt{3} \times 10^{-2}$ and $\nu = 1/\sqrt{3} \times 10^{-4}$. The corresponding Reynolds number and Mach number are $\text{Re} = U_0 L/\nu = 100$ and $\text{Ma} = U_0/c_s = 0.01$, respectively. The initial distribution function is computed from the Chapman-Enskog expansion at the Navier-Stokes order [28]

$$f_\alpha(\boldsymbol{x}, 0) = f_\alpha^{\text{eq}} - \tau \left(\partial_t f_\alpha^{\text{eq}} + \boldsymbol{\xi}_\alpha \cdot \boldsymbol{\nabla}_x f_\alpha^{\text{eq}}\right), \tag{48}$$

where the equilibrium distribution functions are evaluated from the initial analytical solution.

Table 1: L_2-errors and orders of convergence of the velocity field for the Taylor-Green vortex flow using DUGKS and Bardow's scheme.

	N	16	32	64	128
DUGKS	$E_u(t_c)$	4.1E-03	1.1E-03	2.7E-04	6.1E-05
	order	-	1.93	2.02	2.13
Bardow's scheme	$E_u(t_c)$	1.7 E-02	4.4E-03	1.1E-03	2.7E-04
	order	-	1.95	2.00	2.03

We first evaluate the spatial accuracy of DUGKS and Bardow's scheme by simulating the flow with varies mesh sizes ($N \times N$). As we are analyzing the spatial accuracy, the time step is set to a very small value ($\Delta t = 2\tau$) to suppress the errors caused by the time step size. The L_2-error of the velocity field is measured,

$$E_u(t) = \frac{\sqrt{\sum_{x,y} |\boldsymbol{u}_n(x, y, t) - \boldsymbol{u}_a(x, y, t)|^2}}{\sqrt{\sum_{x,y} |\boldsymbol{u}_a(x, y, t)|^2}}, \tag{49}$$

where $\boldsymbol{u}_a$ and $\boldsymbol{u}_n$ are the analytical solution and numerical solution respectively. The L_2-errors at the half-life time $t_c = \ln(2)/(8\nu\pi^2)$ using the two schemes are listed in Table 1. It can be seen that both of the schemes are of second order accuracy in space. But the errors computed from DUGKS results are smaller than those of Bardow's scheme on the same mesh resolutions.
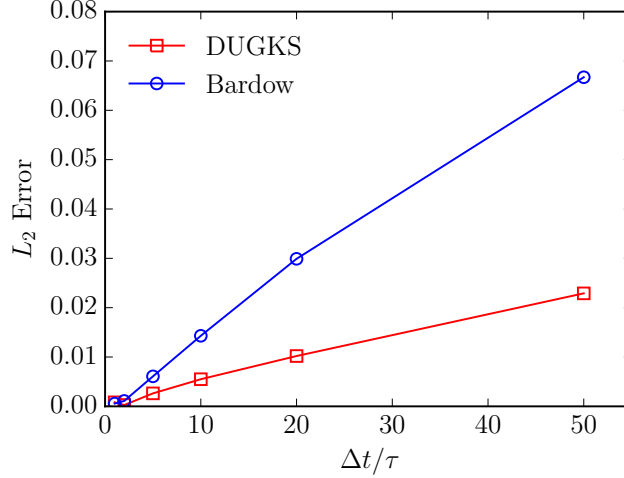
Figure 4: L_2 errors of the velocity field at t_c using varies $\Delta t/\tau$ on a 64×64 mesh.

Since Both the DUGKS and Bardow's scheme can admit a time step larger than the relaxation time, we now investigate their performance at large values of $\Delta t/\tau$. We fix the mesh size ($N = 64$) and the relaxation time but change the time step. The L_2-errors at t_c are shown in Fig. 4, from which we can see that the errors scale almost linearly with the time step size for both methods. Particularly, the two methods still give reasonably accurate results $\Delta t/\tau$ is as large as 50, as shown in Fig. 5. And again, the errors of the DUGKS are smaller than those of Bardow's scheme in all cases. The two methods both blow up as $\Delta t/\tau = 100$ since the CFL number goes beyond 1 at this condition.
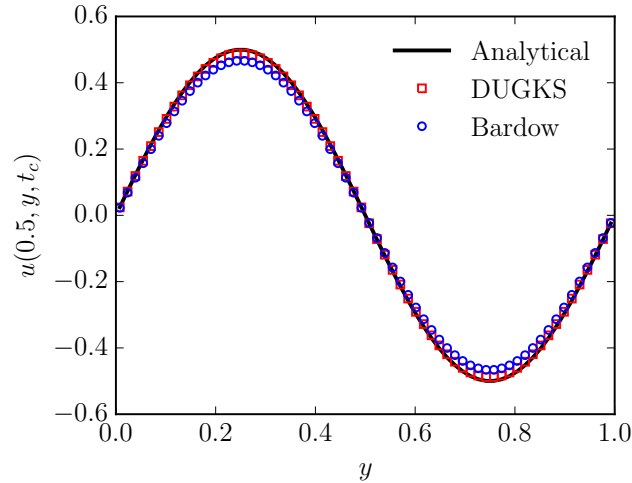
Figure 5: Velocity profile along the line $x = 0.5$ at t_c on a 64×64 mesh with time step $\Delta t = 50\tau$.

Here, we also discuss the computational efficiencies of DUGKS and Bardow's scheme when implementing both of them in FV framework. Their only difference is the computing of numerical flux. But DUGKS introduces two sets of additional DFs and needs to evaluate macro variables at cell in-

terfaces. Thus it can be expected that the DUGKS's computing cost is higher than that of Bardow's scheme. Both of the codes are run on an Intel Xeon E5-2670v3@2.6GHz CPU, the computation time for 10,000 evolution steps using Bardow's scheme and DUGKS with the 64×64 mesh are 10.5s and 19.7s respectively, meaning DUGKS is twice as expensive as Bardow's scheme.

3.2. Lid-driven cavity flow

Incompressible two dimensional lid-driven cavity flow is a popular benchmark problem for numerical schemes. Here, we use it to evaluate the accuracy and stability of the two schemes at different Reynolds numbers. The flow domain is a square cavity with side length L. The top wall moves with a constant velocity U_w, while other walls are kept fixed. The Reynolds number is defined as $\mathrm{Re} = U_\mathrm{w}L/\nu$ with ν being the viscosity of the fluid. In the computation, we set $L = 1$, $U_\mathrm{w} = 0.1$, and the viscosity of the fluid is adjusted to achieve different Reynolds numbers. Uniform Cartesian meshes with grid number $N \times N$ are used in our simulations.
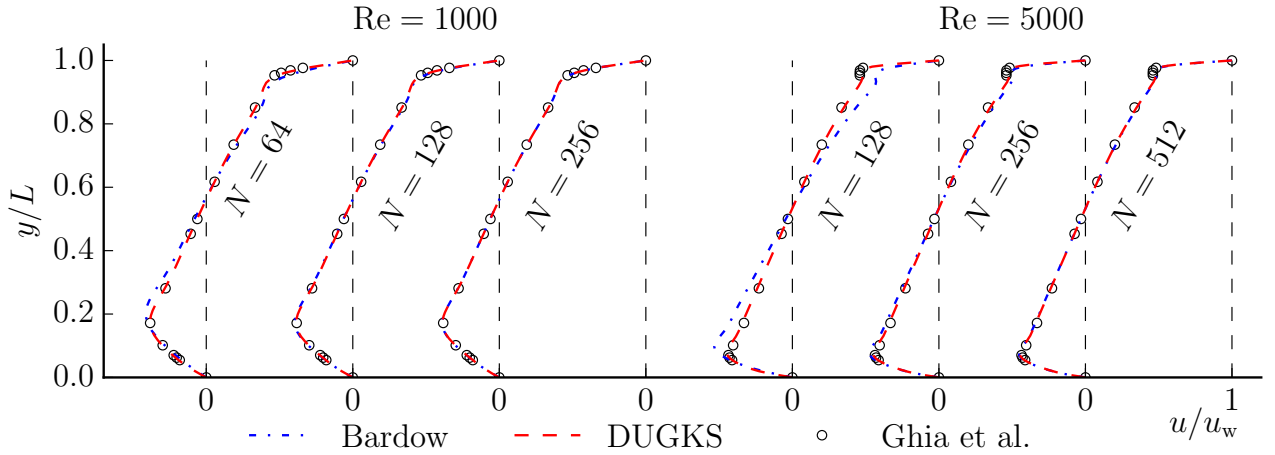

Figure 6: u-velocity profiles along the vertical line passing through the center cavity at $\mathrm{Re} = 1000$ and $\mathrm{Re} = 5000$ using varies mesh size.

We first simulate the flow at $\mathrm{Re} = 1000$ and 5000 with different mesh sizes to compare the accuracy DUGKS and Bardow's scheme in detail. The horizontal (vertical) velocity profiles at steady states along the vertical (horizontal) line passing through the center of cavity predicted by the two schemes using different mesh resolutions are presented in Figs. 6 (7). The benchmark solutions of Ghia et al. [44] are also included for comparison. We can observe that with sufficiently refined meshes ($N = 256$ for $\mathrm{Re} = 1000$, $N = 512$ for $\mathrm{Re}=5000$), the velocity profiles predicted by Bardow's scheme and DUGKS are almost coincident and agree well with the benchmark solutions. When coarser meshes are used, however, the velocity profiles obtained by Bardow's scheme deviate from the benchmark solution obviously. Specifically, the horizontal velocity profiles in the boundary layer near the top wall departure
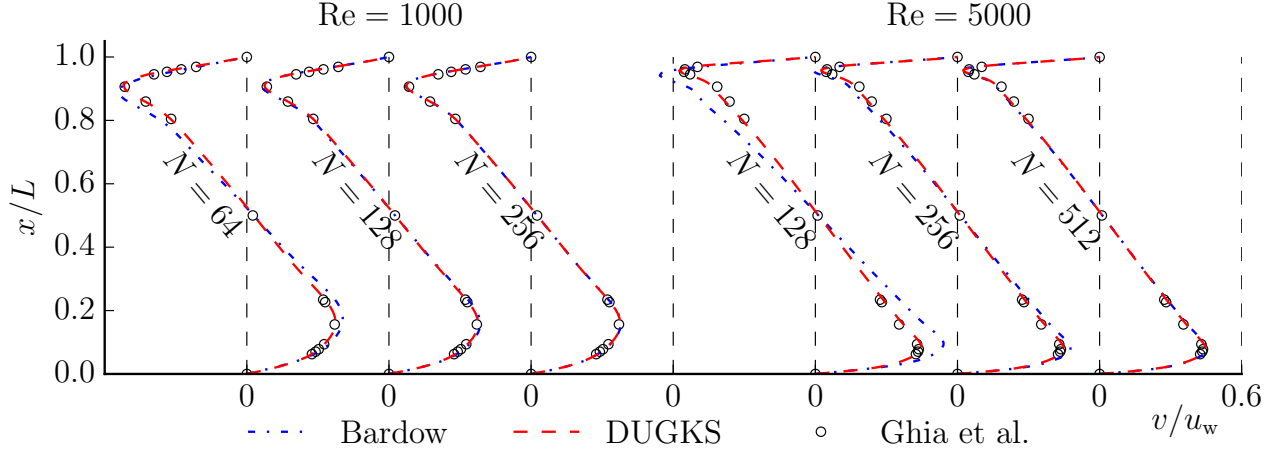
Figure 7: v-velocity profiles along the vertical line passing through the center cavity at Re $= 1000$ and Re $= 5000$ using varies mesh size.

from the benchmark solutions severely at high Reynolds numbers with coarser meshes, which was also observed in Ref. [23]. Contrary to Bardow's scheme, the profiles predicted by DUGKS still match the benchmark solutions quite well on coarser meshes. These observations are also consistent with the theoretical analysis of the two schemes give in Section 2.4.

To get an overview of the difference in the mesh-size-dependence behaviors of the two scheme, we show the contours of the stream function $\psi(x, y)$ and vorticity $\omega(x, y)$ with different mesh sizes. The stream function ψ are integrated from the velocity fields using Simpson's rule assuming zero value at the left wall. The vorticity ω are calculated from the derivatives of the velocity fields using isotropic second order finite difference scheme [35]. The details of our calculating methods for ψ and ω can be found in Ref. [48] since we followed exactly the procedures described in that work. The contour levels of these plots are kept the same with those in Refs. [44, 45], which are two most referred benchmark-studies. As expected, the overall flow patterns shown in the stream function and vorticity fields also reveal that Bardow's scheme and DUGKS give very similar results on the finest meshes but exhibit clear differences for coarser meshes. Generally, the results obtained by DUGKS is less sensitive to mesh sizes. For example, Fig. 11 indicates that at Re $= 5000$, the vorticity field obtained by DUGKS changes only slightly when the mesh size (N) is increased from 128 to 512. On the contrary, the ω fields given by the Bardow's scheme on the coarser mesh ($N = 128$ and $N = 256$) clearly deviate from the result on the $N = 512$ mesh.

To further compare the flow fields quantitatively, we tabulate the positions of the primary and secondary lower vortex centers in Table 2 and Table 3 together with the intensities of the stream function ψ and vorticity ω at the vortex centers. The corresponding benchmark results in the literature [44, 45, 46, 47, 48] are also listed in the tables. For the case of Re $= 1000$, Botella's results [45] are
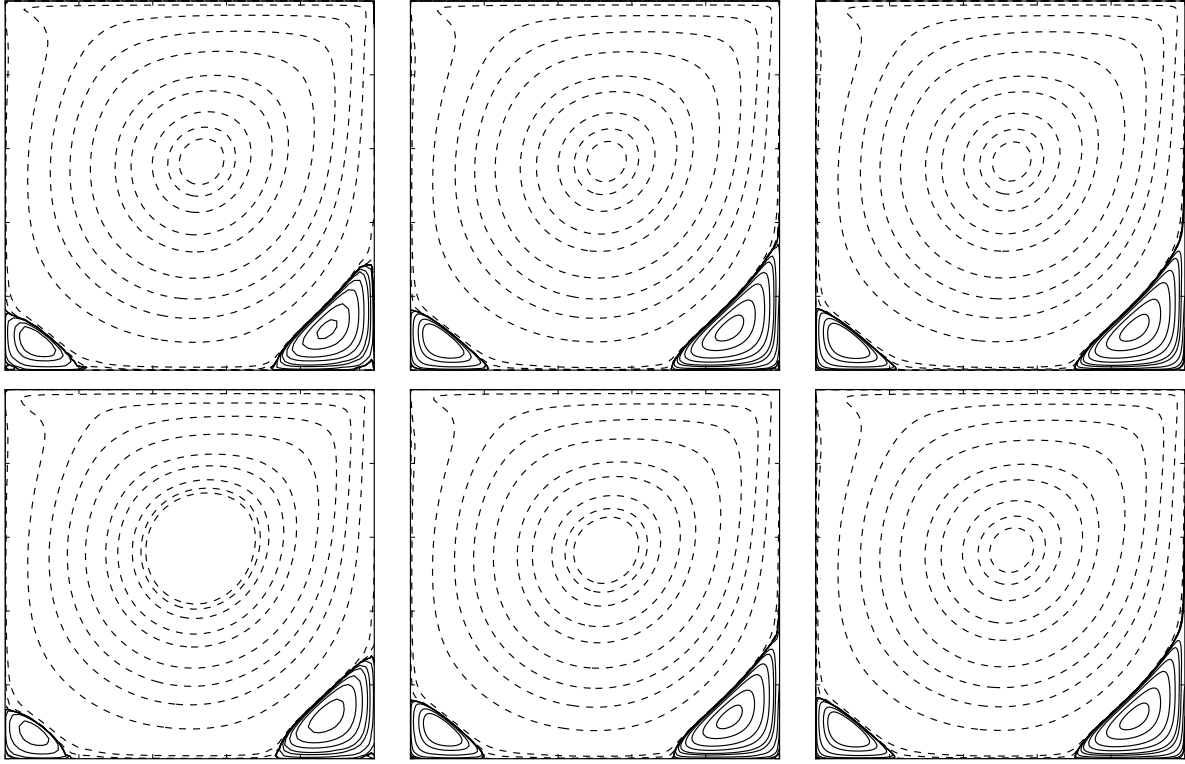
Figure 8: Contours of stream function ψ at the case of Re = 1000 using different methods and varies mesh sizes. Top panel: DUGKS. Bottom panel: Bardow's scheme. Mesh size (N) from left to right: 64, 128 and 256. Solid and dashed lines represent positive and negative values of ψ, respectively.

thought to be highly accurate which were obtained based on a spectral Chebyshev method with special treatment to the singularities at the upper corners of the cavity and the results exhibit a good grid convergence [45]. While for the case of Re = 5000, highly accurate results are rare in the literature.

From Table 2, we can see that for the case of Re = 1000, the primary vortex center position and stream function ψ predicated by DUGKS on the $N = 256$ mesh agree very well (have 4 identical significant figures) with the Botella's solutions, while the vortex intensity $|\omega|$ is 1.2% higher than Botella's. This relative higher discrepancy of ω confirms the statement of Gupta et al. [49] that the vorticity at vortex center is sensitive to the accuracy of wall boundary condition. On the other hand, Bardow's scheme gives quite similar but less accurate results than DUGKS's results on the finest meshes. However, the predicted ψ and ω on coarser meshes deviate quickly even though the vortex center changes only slightly. The obviously larger values of ω at the primary vortex center using coarser meshes are also reflected in Figs. 6 and 7, where the corresponding velocity profiles at the center region are evidently steeper than the benchmark results. In contrast, the results obtained by DUGKS is much less sensitive to mesh sizes. The positions of the lower secondary vortex centers and the values of ψ, ω at the centers presented in Table 3 indicate similar trends.

The above observations confirm that on sufficient refined meshes, the DUGKS and Bardow's scheme

Table 2: Primary vortex center position (x, y) and intensities of the stream function ψ and vorticity ω at the vortex center for the cavity flow.

	N	$(x,$	$y)$	$|\psi|$	$|\omega|$
			Re=1000		
Botella [45]	160	(0.5308,	0.5652)	0.1189336	2.067753
Botella [45]	128	(0.5308,	0.5652)	0.1189336	2.067750
Bruneau [47]	1024	(0.53125,	0.56543)	0.11892	2.0674
Erturk [46]	601	(0.5300,	0.5650)	0.118781	2.065530
Ghia [44]	129	(0.5313,	0.5625)	0.117929	2.04968
Luo [48]	513	(0.531189,	0.566277)	0.118919	2.067664
Luo [48]	257	(0.531128,	0.562257)	0.118843	2.067339
DUGKS	256	(0.530835,	0.565225)	0.118918	2.070272
DUGKS	128	(0.531099,	0.565133)	0.119010	2.070062
DUGKS	64	(0.532409,	0.565339)	0.119478	2.078209
Bardow	256	(0.530716,	0.565158)	0.119345	2.077665
Bardow	128	(0.530339,	0.565303)	0.121681	2.122352
Bardow	64	(0.530152,	0.571904)	0.130824	2.385955
			Re=5000		
Bruneau	2048	(0.51465,	0.53516)	0.12197	1.9327
Erturk	601	(0.5150,	0.5350)	0.121289	1.926601
Ghia	257	(0.5117,	0.5352)	0.118996	1.86016
DUGKS	512	(0.515105,	0.535245)	0.122387	1.945667
DUGKS	256	(0.515335,	0.535248)	0.122665	1.948388
DUGKS	128	(0.516536,	0.535408)	0.123462	1.958624
Bardow	512	(0.514993,	0.535204)	0.123849	1.968384
Bardow	256	(0.514735,	0.535563)	0.130236	2.075018
Bardow	128	(0.514070,	0.538940)	0.150096	2.452553

Table 3: Positions of the lower left and lower right secondary vortex centers and intensities of the stream function ψ and vorticity ω at the vortex centers for the cavity flow. References for the literature data are the same as Table 2.

|	N	Lower-left secondary vortex				Lower-right secondary vortex			
					Re=1000				
		$(x,$	$y)$	$|\psi|\times 10^4$	$|\omega| \times 10$	$(x,$	$y)$	$|\psi|\times 10^3$	$|\omega|$
Botella	160	(0.0833,	0.0781)	2.334528	3.522861	(0.8640,	0.1118)	1.729717	1.109789
Botella	128	(0.0833,	0.0781)	2.334528	3.522832	(0.8640,	0.1118)	1.729717	1.109794
Bruneau	1024					(0.86328,	0.11133)	1.7333	1.1265
Ghia	129	(0.0859,	0.0781)	2.31129	3.6175	(0.85938,	0.1094)	1.75102	1.15465
Erturk	601	(0.0833,	0.0783)	2.3261	3.53473	(0.8633	0.1117)	1.7281	1.115505
Luo	513	(0.082846,	0.078947)	2.331772	3.55657	(0.864522,	0.112086)	1.729537	1.103888
Luo	257	(0.083658,	0.079767)	2.320909	3.65599	(0.861868,	0.110895)	1.729997	1.124101
DUGKS	256	(0.083303,	0.078047)	2.324570	3.503489	(0.863983,	0.111790)	1.737885	1.113440
DUGKS	128	(0.083462,	0.077816)	2.288800	3.460460	(0.865040,	0.111401)	1.731756	1.121638
DUGKS	64	(0.084498,	0.076337)	2.037514	3.212361	(0.871912,	0.110602)	1.645585	1.136373
Bardow	256	(0.083272,	0.078094)	2.320766	3.511439	(0.863929,	0.111679)	1.737000	1.116606
Bardow	128	(0.083055,	0.077727)	2.165012	3.413867	(0.864855,	0.111114)	1.694117	1.121728
Bardow	64	(0.078245,	0.068497)	0.944911	1.999918	(0.871587,	0.113014)	1.370149	0.998399
					Re=5000				
		$(x,$	$y)$	$|\psi|\times 10^3$	$|\omega|$	$(x,$	$y)$	$|\psi|\times 10^3$	$|\omega|$
Ghia	257	(0.0703,	0.1367)	1.36119	1.53055	(0.8086,	0.0742)	3.08358	2.66354
Bruneau	2048					(0.80566,	0.073242)	3.0694	2.7245
Erturk	601	(0.0733,	0.1367)	1.3639	1.502628	(0.8050,	0.0733)	3.0604	2.724481
DUGKS	512	(0.072799,	0.137329)	1.378878	1.521035	(0.804243,	0.072485)	3.090044	2.777576
DUGKS	256	(0.072719,	0.138305)	1.391413	1.532447	(0.804000,	0.071605)	3.135317	2.863107
DUGKS	128	(0.073197,	0.140708)	1.468172	1.586196	(0.811187,	0.071425)	3.459910	3.144925
Bardow	512	(0.072686,	0.137778)	1.385247	1.537686	(0.803505,	0.072074)	3.073734	2.813152
Bardow	256	(0.072965,	0.139162)	1.371750	1.566141	(0.800837,	0.070926)	2.959034	2.960832
Bardow	128	(0.073240,	0.135075)	1.207022	1.377219	(0.805861,	0.076552)	2.837303	3.015223
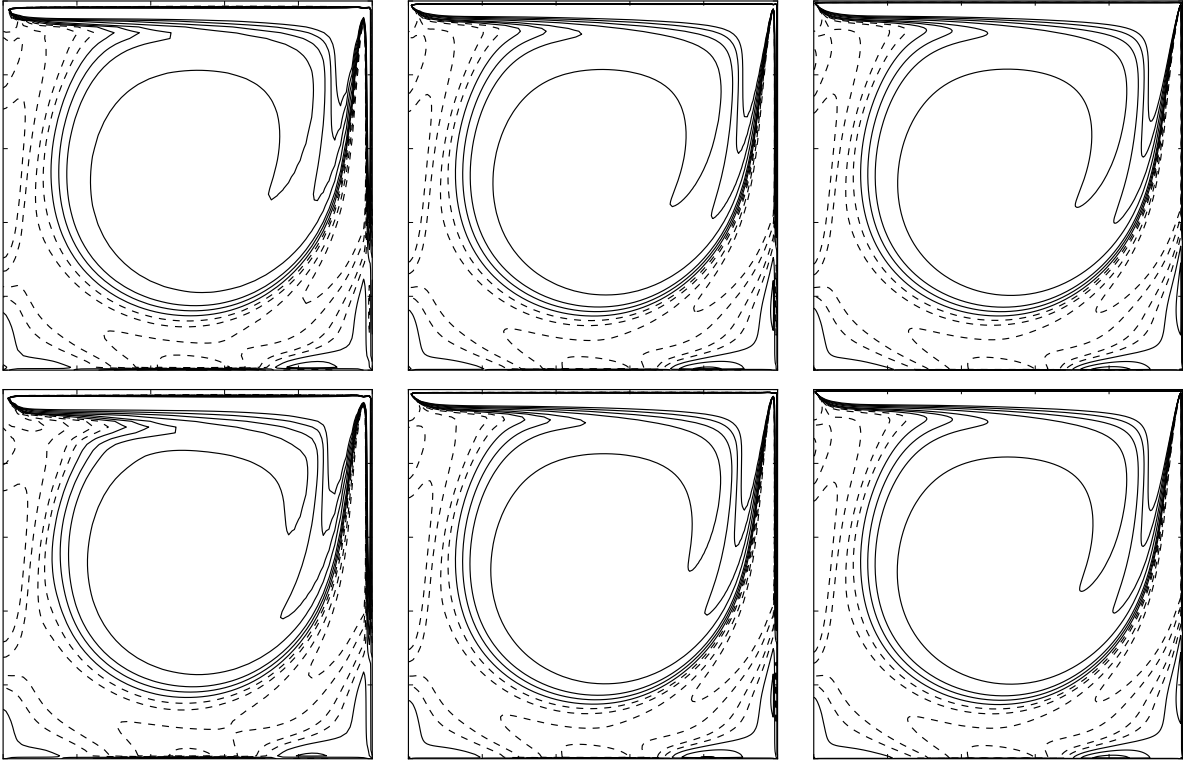
Figure 9: Contours of vorticity function ω at the case of Re = 1000 using different methods and varies mesh sizes. Top panel: DUGKS. Bottom panel: Bardow's scheme. Mesh size (N) from left to right: 64, 128 and 256. Solid and dashed lines represent positive and negative values of ω, respectively.

can give similar results; while with a coarser mesh, DUGKS clearly gives more accurate results than the latter. The results obtained by DUGKS is also less sensitive to mesh resolutions. These results are consistent with the analyses in Sec. 2.4 that evaluating the quadrature of the collision term with a higher order rule can gives more accurate results especially for high Reynolds number flows with wall boundaries.

As has been analyzed in Sec. 2.4, the only difference between DUGKS and Bardow's scheme is the treatment of the integration of the collision term in the evaluation of the cell interface distribution function, and the difference scales with the time step, which have been confirmed in the test of Taylor-Green vortex flow (see Fig. 4). Now we explore the effect of time step on the solution of this steady flow for Bardow's scheme. We simulate the flow at Re = 1000 with the $N = 64$ mesh and 5000 with the $N = 128$ mesh using various CFL numbers. The calculated velocity profiles are shown in Fig. 12. We can see that the errors decrease with decreasing CFL number. But even with CFL=0.1, the errors are still much larger than those of DUGKS.

We also use the cavity flow to assess and compare the stability of the two schemes. Generally, the stability of the numerical schemes for the BGK equation is affected by the treatments of both the advection term and the collision term. The stability for an explicit discretization of the advection term
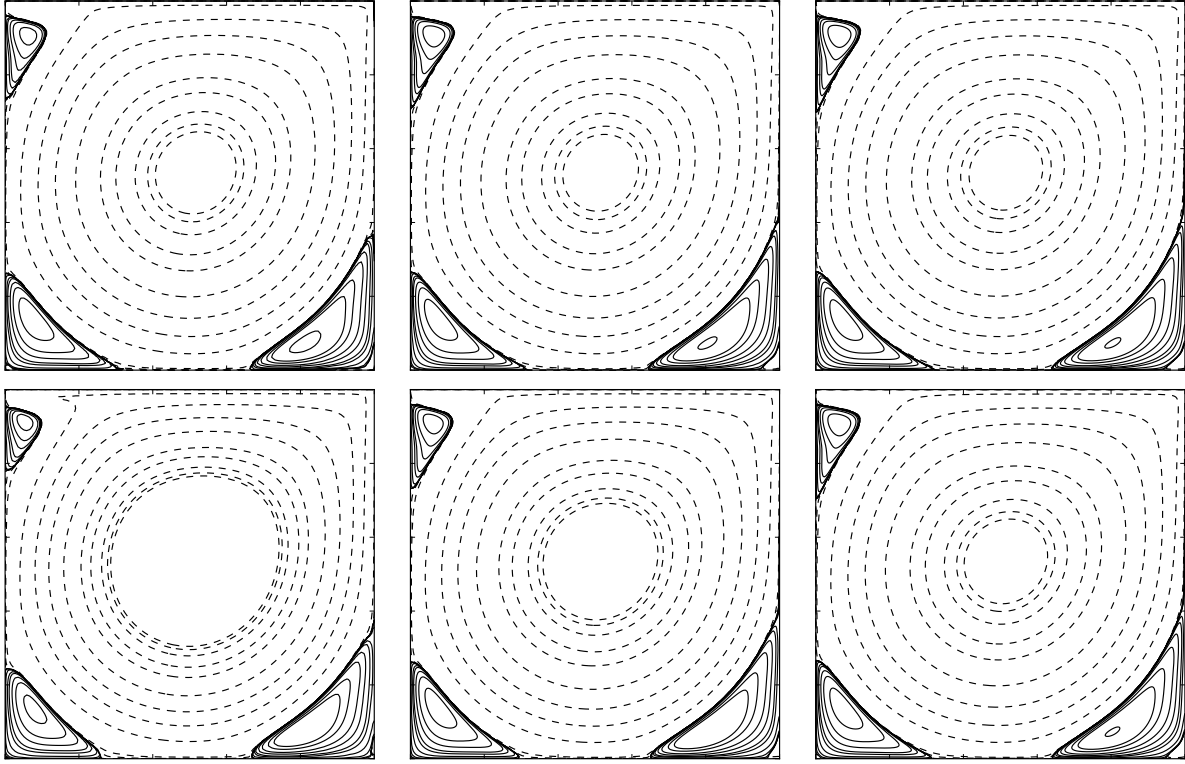
22

Figure 10: Contours of stream function ψ at the case of Re = 5000 using different methods and varies mesh sizes. Top panel: DUGKS. Bottom panel: Bardow's scheme. Mesh size (N) from left to right: 128, 256 and 512. Solid and dashed lines represent positive and negative values of ψ, respectively.

is controlled by the CFL number, while the stability due to the collision term treatment depends on the ratio of Δt and the collision time τ, i.e., $\Delta t/\tau$. The maximum values of $\Delta t/\tau$ at varies CFL numbers for stable computations on the 32×32 and 64×64 meshes are measured and presented in Fig. 13 with error ranges. The figure presents a clear distinction between Bardow's scheme and DUGKS. For Bardow's scheme, the computation is unstable at moderately large $\Delta t/\tau$ even though CFL < 1, while for DUGKS, the stability is almost not affected by the CFL number as long as CFL < 1.1. This observation confirms to the analysis in Sec. 2.4 that the numerical stability is also affected by the treatment of the collision term in the evaluation of numerical flux. Computing the collision term implicitly both in Eq. (10) and Eq. (16) makes DUGKS a rather robust scheme.

3.3. Laminar boundary layer over a flat plate

In the cavity flow, it is observed that Bardow's scheme fails to capture the boundary layer accurately near the top wall of the cavity for large Reynolds numbers. In this subsection, we use the laminar boundary layer flow over a flat plate as a stand-alone case to check this phenomenon and therefore, evaluate the dissipation characteristics of Bardow's scheme and DUGKS. The flow configuration of this problem is sketched in Fig. 14. A uniform flow with horizontal velocity U_0 flows past a flat plate with length L. This steady problem has an analytical self-similar Blasius solution. The Reynolds
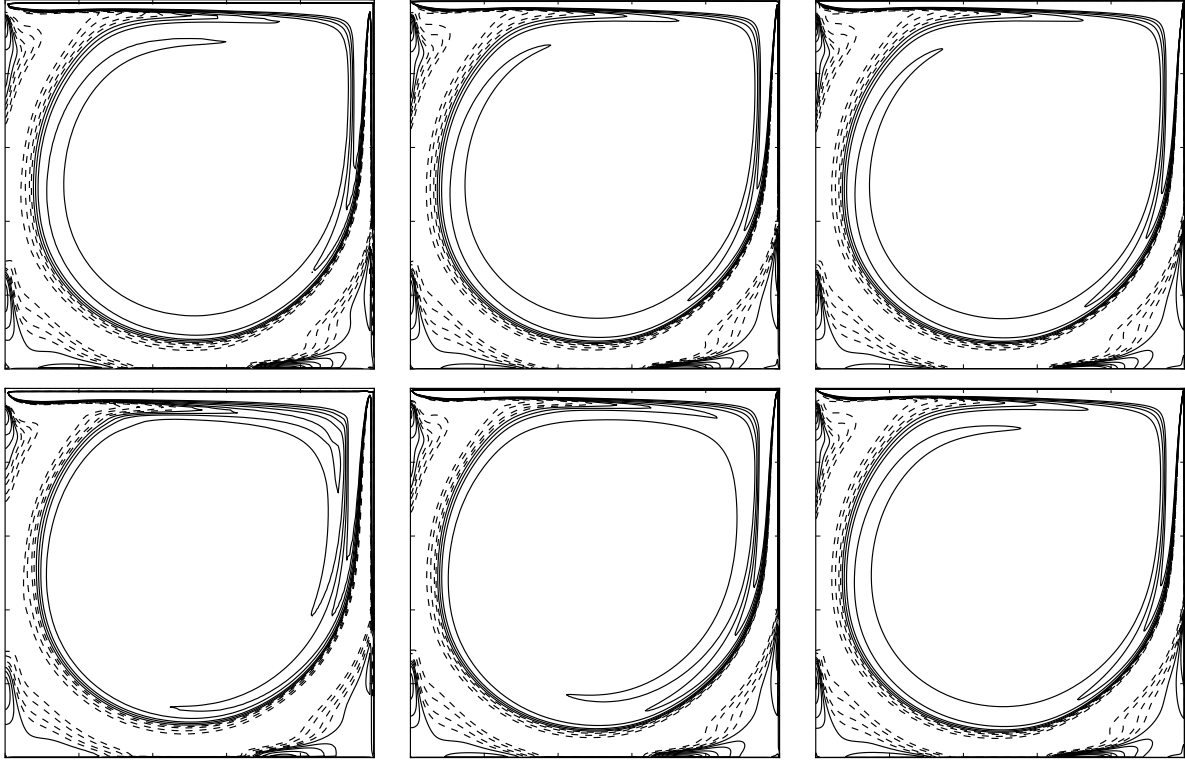
Figure 11: Contours of vorticity function ω at the case of Re = 5000 using different methods and varies mesh sizes. Top panel: DUGKS. Bottom panel: Bardow's scheme. Mesh size (N) from left to right: 128, 256 and 512. Solid and dashed lines represent positive and negative values of ω, respectively.
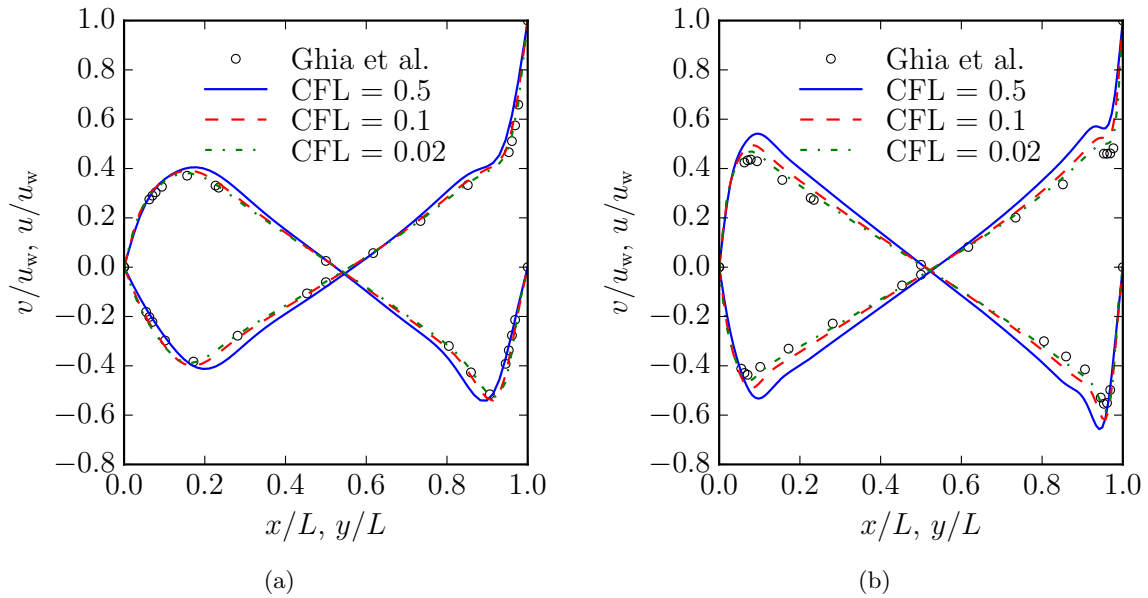

(a)

(b)

Figure 12: Velocity profiles predicted by Bardow's scheme at with different CFL numbers. (a) Re = 1000 on $N = 64$ mesh, (b) Re = 5000 on $N = 128$ mesh.
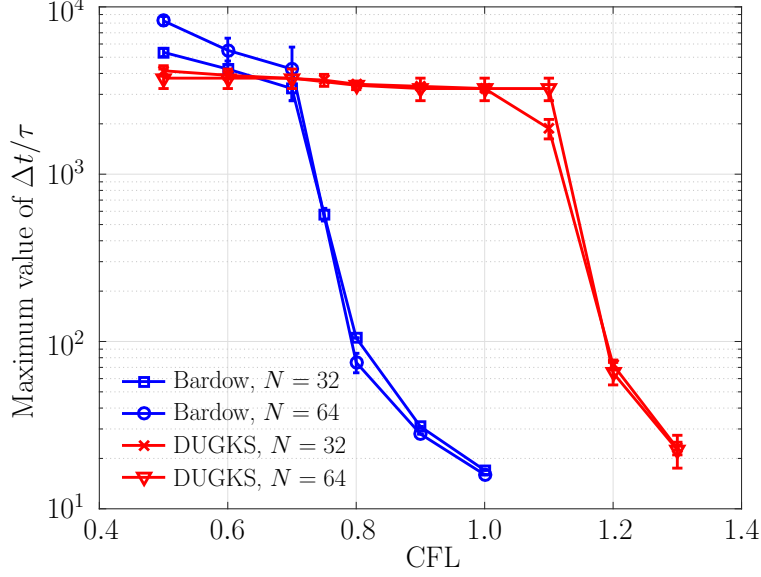
Figure 13: Maximum values of $\Delta t/\tau$ for stable computations of the cavity flow.

number is defined as Re $= U_0 L/\nu$, where ν is the kinematic viscosity. In the simulations, we set $U_0 = 0.1$, $L = 94.76$ and Re $= 10^5$. The boundary layer is very thin at such a high Reynolds number, so non-uniform structured meshes stretched in the vertical direction are employed (Fig.14). The cell size along Y direction increases with a ratio $A_y = 1.1$. The height of the first layer is denoted by $\Delta y_{\min}$. The grid number in the Y direction is adjusted according to $\Delta y_{\min}$ to make sure the height of the computation domain is right beyond 50. The cell size in the X direction is refined at the leading edge of the plate, with $\Delta x_{\min} = 0.1$ to account for the singularity of the flow behavior there. The increasing ratios of the cell size to the downstream and upstream from the leading edge are $A_r = 1.05$ and $A_l = 1.1$, respectively. The total cell number in the X direction is 120, with 80 cells distributed on the plate surface. Free stream condition is applied to the left and top boundaries. Outflow boundary condition is applied to the right boundary, and symmetric boundary condition is used at the section before the plate at the bottom boundary. No-slip boundary condition is imposed at the bottom wall and is realized by the method described in Sec. 2.5.

We simulate the flow with different mesh resolutions by adjusting the parameter $\Delta y_{\min}$ from 0.01 to 0.1. The CFL number is fixed at 0.5. The velocity profiles at $X_1 = 6.4381$ and $X_2 = 21.5082$ predicted by the two schemes together with the Blasius solutions are shown in Figs. 15 and 16. The horizontal velocity is scaled by U_0, and the vertical velocity is scaled by $U_0/2\sqrt{\text{Re}_x}$, where Re_x is the local Reynolds number defined as $U_0 x/\nu$. Note that for the DUGKS, the profiles with the mesh of $\Delta y_{\min} = 0.01$ are not shown for a clear presentation because the profiles at varies meshes are almost overlapped.
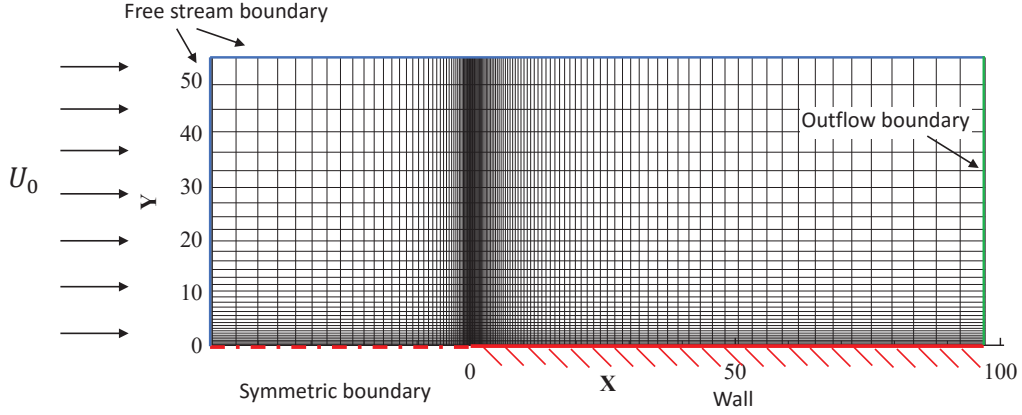
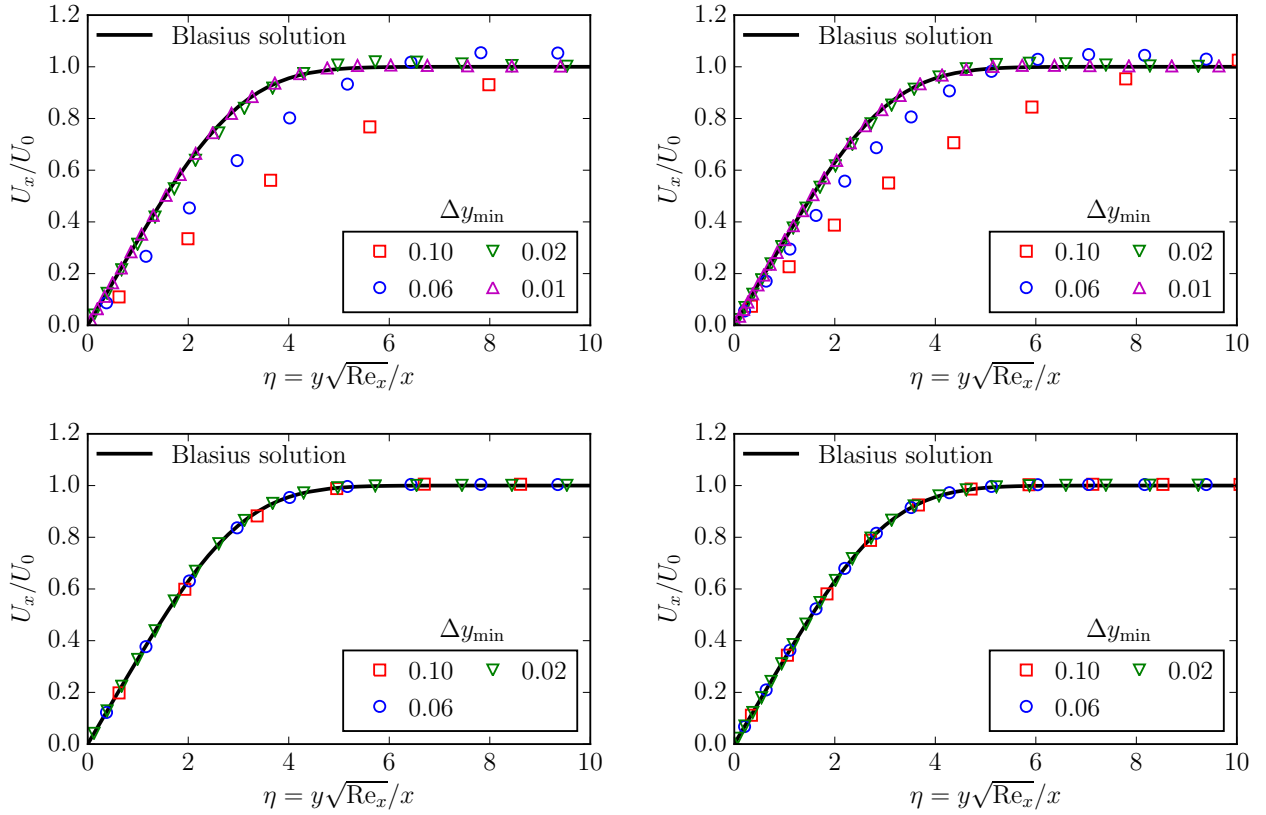Figure 14: Mesh for the laminar boundary layer.

Figure 15: Horizontal velocity profiles in the boundary layer calculated by Bardow's scheme and DUGKS with different mesh resolutions, CFL=0.5. Top: Bardow's scheme; Bottom: DUGKS; Left: results at x=6.4381; Right: results at x=21.5082.
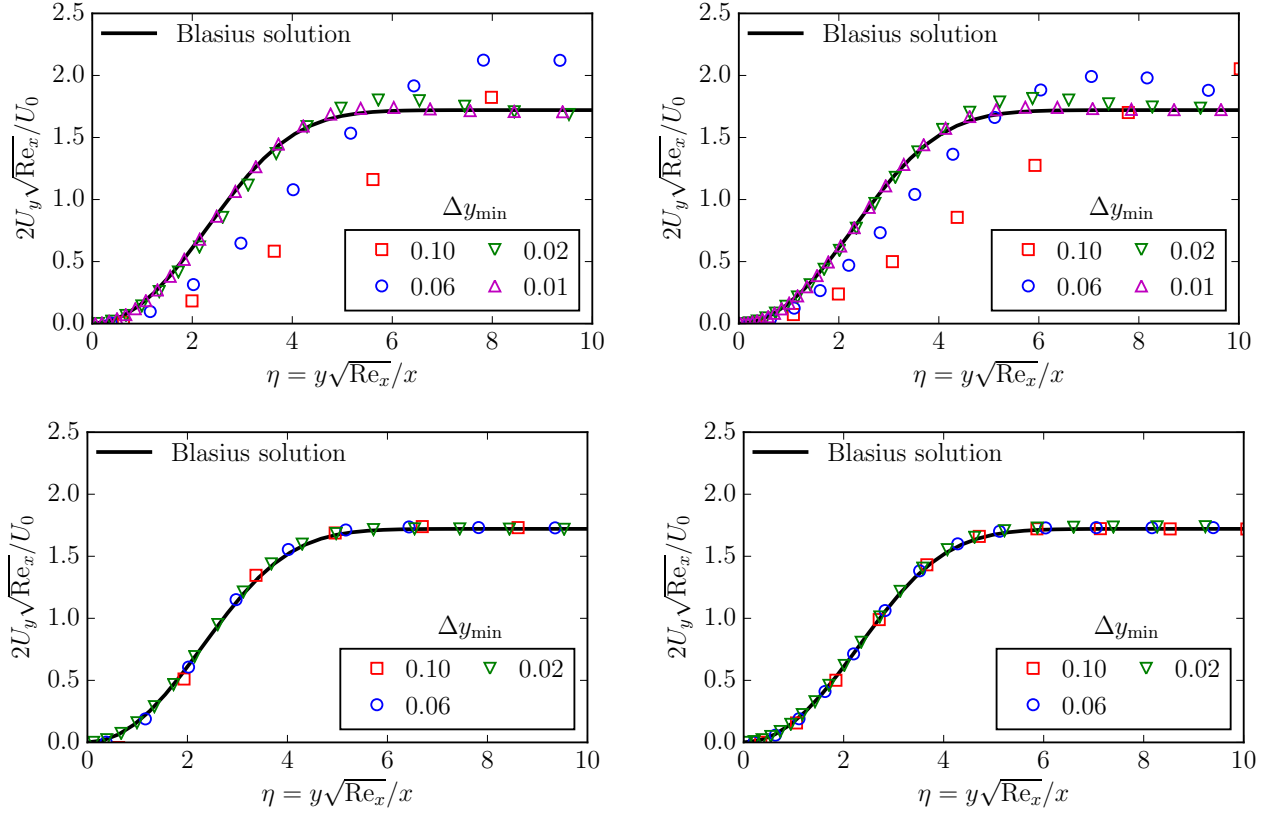
Figure 16: Vertical velocity profiles in the boundary layer calculated by Bardow's scheme and DUGKS with different mesh resolutions, CFL=0.5. Top: Bardow's scheme; Bottom: DUGKS; Left: results at x=6.4381; Right: results at x=21.5082.

From these results, we can observe that, the boundary layer can be captured accurately by DUGKS with the all of these meshes. In particular, with the coarsest mesh ($\Delta y_{\min} = 0.1$), there are only 4 cells in the boundary layer at $x = X_1$. On the other hand, Bardow's scheme only gives satisfactory results with the finest mesh ($\Delta y_{\min} = 0.01$), as shown in Figs. 15 and 16. It is also observed that the results of Bardow's scheme are quite sensitive to the mesh employed. With the coarser meshes, the boundary layer thickness is over predicted, which indicates Bardow's scheme introduces excessive numerical dissipation. While outside the boundary layer, the streamwise velocity is overprotected. This can be explained by the blocking and accelerating effects due to the numerically enlarged boundary layer thickness. We note that such over-predictions were also observed in Refs.[32, 36].
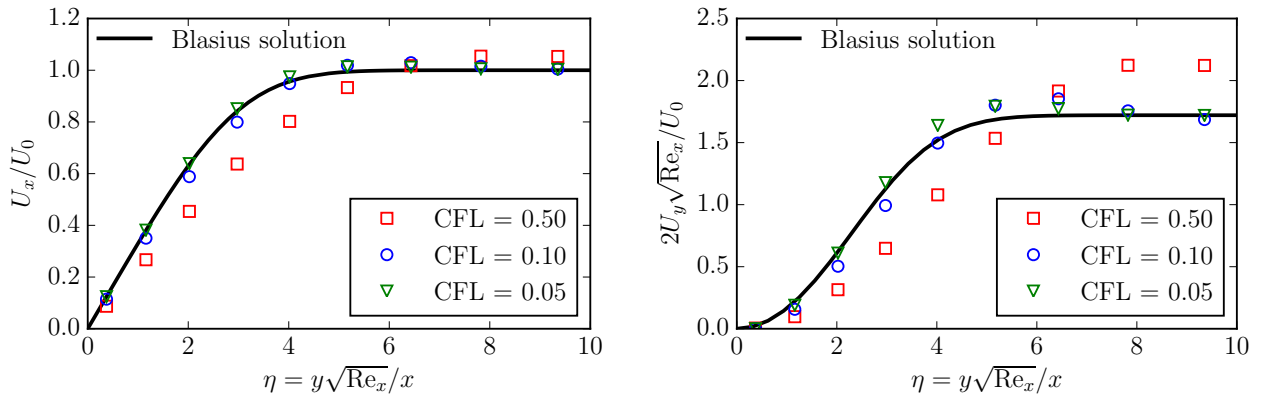

Figure 17: Horizontal (left) and vertical (right) velocity profiles at $x = 21.5082$. for the boundary layer flow case, calculated by Bardow's scheme using $\Delta y_{\min} = 0.1$ and different CFL numbers.

Like the cavity flow case, we reduce the time step in simulation using Bardow's scheme to examine the effects of time step. The computation is carried out on the mesh of $\Delta y_{\min} = 0.1$ and the CFL number varies from 0.5 to 0.05. The velocity profiles are presented in Fig. 17. It can be seen that using of a small time step can improve the accuracy, but the deviations from the Blasius solution are still obvious even with CFL=0.05.

As a reference, we have also simulated this problem using the standard LBM with the single relaxation time approximation (LBKG) model on two uniform meshes with $\Delta y = 0.1$ and $\Delta y = 0.05$, respectively. The computational domain size is 150 in width and 50 in height. Thus the uniform mesh sizes (1500×500 and 3000×1000) are much larger compared with the meshes used in DUGKS and Bardow's scheme. The half-way bounce back scheme is applied to the plate surface. Fig. 18 shows the velocity profiles near $x = 21.5082$ given by the LBM simulations. It can be seen that the LBM results are quite accurate even on the mesh with $\Delta y = 0.1$. We note that for a further coarser mesh with $\Delta y = 0.2$, the computation with LBM becomes unstable, even though we lower the Reynolds number to 10^4 at the early stage of the computation to avoid the quick divergence due to the strong oscillation
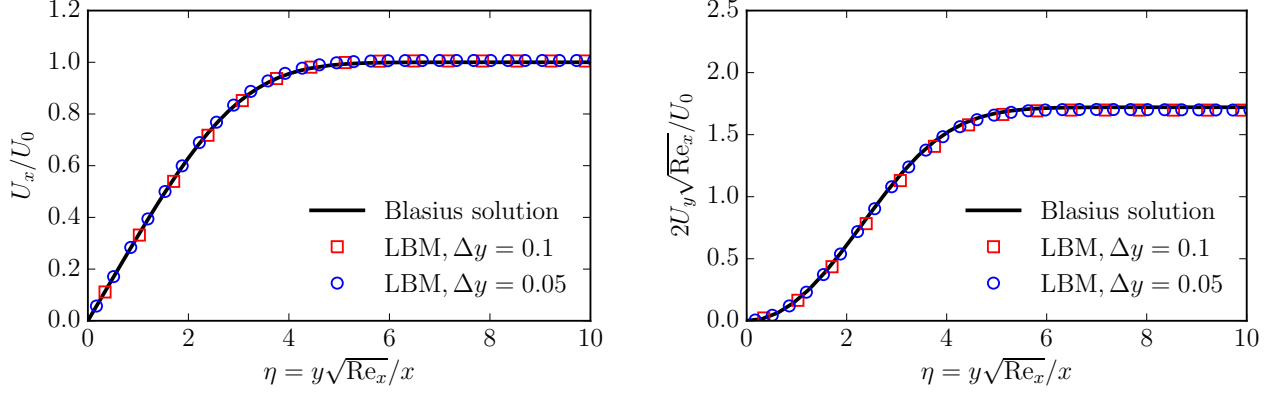
28

Figure 18: Horizontal (left) and vertical (right) velocity profiles near $x = 21.5082$ for the boundary layer flow case, calculated by the standard LBM.

near the plate. But the computation of DUGKS is still stable with this mesh even at $\mathrm{Re} = 10^5$. We here also compare the computation time using the DUGKS with the non-uniform mesh of $\Delta y_{\min} = 0.1$ and the standard LBM with the uniform mesh of $\Delta y = 0.1$. The DUGKS program is a serial one and takes 169s to get the converged solution. While the LBM program is a parallel one running with 48 MPI processes and it takes 277s to get the converged solution. Considering the similar accuracy, and the largely reduced computation time with non-uniform meshes, the DUGKS is a well suited off-lattice Boltzmann scheme for such flows involving boundary layer.

4. Conclusions

In this paper, the performance of two kinetic schemes, i.e., the off-lattice Boltzmann proposed by Bardow et al. and the DUGKS is compared. Both of them can remove the time step restriction which is commonly seen in many off-lattice Boltzmann schemes. A theoretical analysis in the finite-volume framework demonstrates that the two methods differ only in the constructions of numerical flux. Bardow's scheme treats the collision integral with the one-point quadrature when integrate the BGK equation along the characteristic line to evaluate the numerical flux, while DUGKS computes it with the trapezoidal quadrature. Consequently, DUGKS is more accurate and stable than Bardow's scheme.

The numerical results of three test cases, including unsteady and steady flows, confirm that the DUGKS is more accurate and stable than Bardow's scheme on the same computing configurations, especially for high Reynolds number flows. It is also observed that DUGKS is stable as long as CFL < 1, while the stability of Bardow's scheme degrades quickly as the CFL number goes beyond 0.5. We attribute this to the implicit treatment of the collision term of the DUGKS when evaluating the numerical flux. Furthermore, the results show that DUGKS is less sensitive to mesh resolutions

than Bardow's scheme in terms of accuracy. Numerical results also demonstrate that DUGKS is twice as computationally expensive as Bardow's scheme on a same mesh. However, it should be noted that DUGKS can achieve an accurate solution with a much finer mesh, suggesting that it can be more efficient than Bardow's scheme. In summary, the theoretical analysis and numerical results demonstrate that DUGKS can serve as an efficient method for simulating continuum flows, although it is not limited to such flow regime.

Acknowledgments

References

[1] A. Bardow, I.V. Karlin, A.A. Gusev, General characteristic-based algorithm for off-lattice Boltzmann simulations, Euro. Phys. Lett., 75 (2006) 434.

[2] Z.L. Guo, K. Xu, R.J. Wang, Discrete unified gas kinetic scheme for all Knudsen number flows: Low-speed isothermal case, Phys. Rev. E, 88 (2013) 033305.

[3] Z.L. Guo, T.S. Zhao, Y. Shi, Preconditioned lattice-Boltzmann method for steady flows, Phys. Rev. E, 70 (2004) 066706.

[4] K.N. Premnath, M.J. Pattison, S. Banerjee, Steady state convergence acceleration of the generalized lattice boltzmann equation with forcing term through preconditioning, J. Comp. Phys., 228 (2009) 746-769.

[5] D.J. Mavriplis, Multigrid solution of the steady-state lattice Boltzmann equation, Comp. Fluids, 35 (2006) 793-804.

[6] D.V. Patil, K.N. Premnath, S. Banerjee, Multigrid lattice Boltzmann method for accelerated solution of elliptic equations, J. Comput. Phys., 265 (2014) 172-194.

[7] X.W. Shan, X.Y. He, Discretization of the velocity space in the solution of the Boltzmann equation, Phys. Rev. Lett., 80 (1998) 65-68.

[8] X.W. Shan, X.-F. Yuan, H.D. Chen, Kinetic theory representation of hydrodynamics: A way beyond the Navier-Stokes equation, J. Fluid Mech., 550 (2006) 413-441.

[9] W.P. Yudistiawan, S.K. Kwak, D.V. Patil, S. Ansumali, Higher-order Galilean-invariant lattice Boltzmann model for microflows: Single-component gas, Phys. Rev. E, 82 (2010) 046701.

[10] J.P. Meng, Y.H. Zhang, Gauss-Hermite quadratures and accuracy of lattice Boltzmann models for nonequilibrium gas flows, Phys. Rev. E, 83 (2011) 036704.

[11] F. Nannelli, S. Succi, The lattice Boltzmann equation on irregular lattices, J. Stat. Phys., 68 (1992) 401-407.

[12] M. Stiebler, J. Tölke, M. Krafczyk, An upwind discretization scheme for the finite volume lattice Boltzmann method, Comput. Fluids, 35 (2006) 814-819.

[13] R. Mei, W. Shyy, On the finite difference-based lattice Boltzmann method in curvilinear coordinates, J. Comput. Phys., 143 (1998) 426-448.

[14] G. Peng, H. Xi, C. Duncan, S.-H. Chou, Finite volume scheme for the lattice Boltzmann method on unstructured meshes, Phys. Rev. E, 59 (1999) 4675-4682.

[15] T. Lee, C.-L. Lin, A characteristic Galerkin method for discrete Boltzmann equation, J. Comput. Phys., 171 (2001) 336-356. meirw98

[16] T. Lee, C.-L. Lin, An Eulerian description of the streaming process in the lattice Boltzmann equation, J. Comput. Phys., 185 (2003) 445-471.

[17] Z.L. Guo, T.S. Zhao, Explicit finite-difference lattice Boltzmann method for curvilinear coordinates, Phys. Rev. E, 67 (2003) 066709.

[18] N. Rossi, S. Ubertini, G. Bella, S. Succi, Unstructured lattice Boltzmann method in three dimensions, Int. J. Numer. Meth. Fluids., 49 (2005) 619-633.

[19] A. Bardow, I.V. Karlin, A.A. Gusev, Multispeed models in off-lattice Boltzmann simulations, Phys. Rev. E, 77 (2008) 025701.

[20] D.V. Patil, K.N. Lakshmisha, Finite volume TVD formulation of lattice Boltzmann simulation on unstructured mesh, J. Comput. Phys., 228 (2009) 5262-5279.

[21] G.R. McNamara, A.L. Garcia, B.J. Alder, Stabilization of thermal lattice Boltzmann models, J. Stat. Phys., 81 (1995) 395-408.

[22] Z.L. Guo, C.G. Zheng, T.S. Zhao, A lattice BGK scheme with general propagation, J. Sci. Comput., 16 (2001) 569-585.

[23] P.R. Rao, L.A. Schaefer, Numerical stability of explicit off-lattice Boltzmann schemes: A comparative study, J. Comput. Phys., 285 (2015) 251-264.

[24] Z.L. Guo, R.J. Wang, K. Xu, Discrete unified gas kinetic scheme for all Knudsen number flows. II. Thermal compressible case, Phys. Rev. E, 91 (2015) 033313.

[25] P. Wang, L.H. Zhu, Z.L. Guo, K. Xu, A comparative study of LBE and DUGKS methods for nearly incompressible flows, Commun. Comput. Phys., 17 (2015) 657-681.

[26] L.H. Zhu, Z.L. Guo, K. Xu, Discrete unified gas kinetic scheme on unstructured meshes, Comput. Fluids, 127 (2016) 211-225.

[27] P.L. Bhatnagar, E.P. Gross, M. Krook, A model for collision processes in gases. I. Small amplitude processes in charged and neutral one-component systems, Phys. Rev., 94 (1954) 511.

[28] Z.L. Guo, C. Shu, Lattice Boltzmann Method and Its Applications in Engineering, World Scientific, Singapore, 2013.

[29] D.V. Patil, Chapman-Enskog analysis for finite-volume formulation of lattice Boltzmann equation, Physica A, 392 (2013) 2701-2712.

[30] V. Sofonea, R. F. Sekerka, Viscosity of finite difference lattice Boltzmann models, J. Comput. Phys., 184 (2003) 422-434.

[31] S.H. Kim, H. Pitsch, I.D. Boyd, Accuracy of higher-order lattice Boltzmann methods for microscale flows with finite Knudsen numbers, J. Comput. Phys., 227 (2008) 8655-8671.

[32] W.D. Li, L.-S. Luo, Finite volume lattice Boltzmann method for near incompressible flows on arbitrary unstructured meshes, Commun. Comput. Phys, 20 (2016), 301-324.

[33] Y. Wang, C. Shu, H. Huang, C. Teo, Multiphase lattice Boltzmann flux solver for incompressible multiphase flows with large density ratio, J. Comput. Phys., 280 (2015) 404-423.

[34] R.J. LeVeque, Finite Volume Methods for Hyperbolic Problems, Cambridge University Press, Cambridge, 2002.

[35] A. Kumar, Isotropic finite-differences, J. Comput. Phys., 201 (2004) 109-118.

[36] S. Ubertini, G. Bella, S. Succi, Lattice Boltzmann method on unstructured grids: further developments, Phys. Rev. A 68 (2003) 016701

[37] M.K. Misztal, A. Hernandez-Garcia, R. Matin, H.O. Sørensen, J.Mathiesen, Detailed analysis of the lattice Boltzmann method onunstructured grids, J. Comput. Phys., 297 (2015) 316-339.

[38] T. Ohwada, On the construction of kinetic schemes, J. Comput. Phys., 177 (2002) 156-175.

[39] S. Chen, K. Xu, A comparative study of an asymptotic preserving scheme and unified gas-kinetic scheme in continuum flow limit, J. Comput. Phys., 288 (2015) 52-65.

[40] K. Xu, Z. Li, Dissipative mechanism in Godunov type schemes, Int. J. Numer. Meth. Fluids, 37 (2001) 1-22.

[41] K. Xu, A Gas-Kinetic BGK scheme for the Navier-Stokes equations and its connection with artificial dissipation and Godunov method, J. Comput. Phys., 171 (2004) 289-335.

[42] C. Wu, B.C. Shi, Z.H. Chai, P. Wang, Discrete unified gas kinetic scheme with a force term for incompressible fluid flows, Comput. Math. Appl., 71 (2016) 2608-2629.

[43] X.Y. He, X.W. Shan, G.D. Doolen, Discrete Boltzmann equation model for nonideal gases, Phys. Rev. E 57 (1998), 13-16

[44] U. Ghia, K.N. Ghia, C.T. Shin, High-Re solutions for incompressible flow using the Navier-Stokes equations and a multigrid method, J. Comput. Phys., 48 (1982) 387-411.

[45] O. Botella, R. Peyret, Benchmark spectral results on the lid-driven cavity flow, Comput. Fluids, 27 (1998) 421-433.

[46] E. Erturk, T.C. Corke, C. Gökçöl, Numerical solutions of 2-D steady incompressible driven cavity flow at high Reynolds numbers, Int. J. Numer. Meth. Fluids, 48 (2005) 747-774.

[47] C.-H. Bruneau, M. Saad, The 2D lid-driven cavity problem revisited, Comput. Fluids, 35 (2006) 326-348.

[48] L.-S. Luo, W. Liao, X. Chen, Y. Peng, W. Zhang, Numerics of the lattice Boltzmann method: Effects of collision models on the lattice Boltzmann simulations, Phys. Rev. E, 83 (2011) 056710.

[49] M.M. Gupta, R.P. Manohar, Boundary approximations and accuracy in viscous flow computations, J. Comput. Phys., 31(1979) 265-288.

[50] P.K. Knudu, I.M. Cohen, D.R. Dowling, Fluid Mechanics 5th ed., Elsevier, Singapore, 2012.